Subcell-resolution finite-difference modelling of seismic waves in Biot and JKD poroelastic media

David Gregor,[1] Peter Moczo [1,2] Jozef Kristek [1,2] Arnaud Mesgouez,[3]
Gaëlle Lefeuve-Mesgouez[3] and Miriam Kristekova [1,2]

[1] *Faculty of Mathematics, Physics and Informatics, Comenius University Bratislava, Mlynska dolina F*1, 842 48 *Bratislava, Slovak Republic.*
E-mail: *moczo@fmph.uniba.sk*
[2] *Earth Science Institute, Slovak Academy of Sciences, Dubravska cesta* 9, 845 28 *Bratislava, Slovak Republic*
[3] *Avignon Université, INRAE, UMR EMMAH, BP*21239, *F-*84911 *Avignon, France*

SUMMARY
We present a discrete representation of strongly heterogeneous poroelastic medium with the JKD-model of the frequency-dependent permeability and resistive friction, and the corresponding finite-difference (FD) scheme for numerical modelling of seismic wave propagation and earthquake ground motion in structurally complex media. The scheme is capable of subcell resolution, that is, allows for an arbitrary shape and position of an interface in the spatial grid. The medium can have either a zero resistive friction or non-zero constant resistive friction or JKD frequency-dependent resistive friction. The scheme has the same computational efficiency as the scheme for a smoothly and weakly heterogeneous medium (medium without material interfaces) because the number of operations for updating wavefield is the same. Several comparisons with a semi-analytical approach proves the efficiency and reliability of the subcell-resolution FD scheme. An illustrative example demonstrates differences between earthquake ground motion in the Biot's and JKD variants of the model of the surface sedimentary basin. The example indicates that it is desirable to perform an extensive parametric study in order to find out when it is necessary to apply relatively complicated and computationally more demanding JKD model and when much simpler Biot's model is sufficient.

Key words: Permeability and porosity; Numerical approximations and analysis; Computational seismology; Earthquake ground motions; Site effects; Theoretical seismology; Wave propagation.

1 INTRODUCTION

Moczo *et al.* (2019) developed a discrete grid representation of a strongly heterogeneous poroelastic medium with zero or non-zero constant (frequency independent) resistive friction for the finite-difference (FD) modelling of seismic wave propagation. The representation makes it possible (i) to model an arbitrary shape and position of a material interface in the spatial grid with subcell resolution, (ii) to keep computational efficiency of the FD scheme for a homogeneous or smoothly and weakly heterogeneous medium. The latter property is because the number of algebraic operations for updating stress-tensor, fluid pressure, and the solid and fluid particle velocities in the scheme for the discrete representation of the strongly heterogeneous medium (including material interfaces) is the same as that for the homogeneous or smoothly and weakly heterogeneous medium. The only difference is that it is necessary to evaluate averaged grid material parameters once before the FD simulation itself.

Approximately, the Biot's characteristic frequency separates the so-called low-frequency and high-frequency regimes of wave propagation in the poroelastic medium. At low frequencies, that is at frequencies sufficiently lower than the Biot's characteristic frequency, it is possible to consider a non-zero frequency-independent resistive friction. At high frequencies it is necessary to consider a frequency-dependent resistive friction. Johnson, Koplik & Dashen (1987) developed a model (now called the JKD model) of the poroelastic medium with frequency-dependent dynamic permeability that is not restricted to either low or high frequencies. The frequency-dependent permeability implies frequency-dependent resistive friction.

1.1 Our goal

It is logical to extend the methodology presented by Moczo *et al.* (2019) to the JKD model of the poroelastic medium. Such an extension will make it possible to apply the FD modelling with the sub-cell resolution capability to strongly heterogeneous poroelastic media in any frequency range with respect to the Biot's characteristic frequency. One specific example is the earthquake ground motion in surface sediments with high permeability. In the highly permeable sediments, the Biot's characteristic frequency can be relatively close to the earthquake ground motion and earthquake-engineering frequency range of interest.

1.2 FD modelling in the poroelastic medium

Since Moczo *et al.* (2019) presented a relatively detailed overview of the FD modelling of seismic wave propagation in the poroeleastic medium, we just briefly comment important contributions which were not mentioned in the above paper.

Itzá *et al.* (2016) applied the global optimal implicit staggered-grid FD scheme based on the least-squares approach, proposed originally by Liu (2014) for the elastic medium, to 2-D porous media. Balam *et al.* (2018) incorporated the above FD scheme into the self-organizing maps of the neural network algorithm to obtain synthetic waveforms in poroelastic media for reservoir modelling. Zhang, *et al.* (2017) developed explicit flat-free-surface boundary condition for modelling seismic wave propagation in the poroelastic medium using the staggered-grid FD scheme. A recent and very valuable contribution to the FD modelling of seismic wave propagation in poroelastic medium is presented in the paper by Sun *et al.* (2019). Sun *et al*. developed a modification of the traction-imaging scheme developed originally by Zhang & Chen (2006) and Zhang *et al*. (2012) for modelling seismic wave propagation in elastic models with non-planar free surface. Sun *et al.* (2019) extended the approach to the poroelastic medium. They expressed equations of Biot's theory in curvilinear coordinates and solved them on the collocated grid using the 4th-order accurate Runge–Kutta scheme with alternating applications of the forward and backward MacCormack FD approximations. They derived formulas of the free-surface boundary conditions for the poroelastic medium in the curvilinear coordinates and subsequently implemented them with the traction-imaging method.

1.3 Analytical and semi-analytical methods and solutions

Usually, the analytical and semi-analytical solutions are restricted to structurally and/or rheologically simple models. However, just due to these restrictions they are very useful in investigating physics of seismic wave propagation using fundamental canonical models. At the same time, analytical and semi-analytical solutions are indispensable in verifying the approximate numerical-modelling methods.

Comprehensive reviews of the analytical and semi-analytical solutions for elastic wave propagation in the poroelastic medium can be find in, for example Karpfinger *et al.* (2009), Schanz (2009) and Cheng (2016). Here we mention just one method developed by Mesgouez & Lefeuve-Mesgouez (2009) because we will directly use the method to verify the FD modelling. Mesgouez & Lefeuve-Mesgouez (2009) derived the semi-analytical solution for a model consisting of horizontal poroelastic layers over a poroelastic half-space. The wavefield is excited by a vertically polarized load (acting on a strip) at the free surface. Mesgouez & Lefeuve-Mesgouez (2009) used the exact stiffness matrix method for the Biot's theory coupled with a matrix conditioning technique. The solution is developed at first in the wavenumber–frequency domain and can be transformed into the space–time domain using Fourier transforms. The equations of motion contain frequency-dependent dynamic permeability $\kappa(\omega)$. The solution can be expressed in terms of any poroelastic field variable.

1.4 Structure of this paper

We can outline the structure of this paper:

(1) constitutive relations for the smoothly heterogeneous poroelastic medium and the averaged poroelastic medium representing possibly strongly heterogeneous medium with material interfaces,
(2) equations of motion for the medium with a constant resistive friction,
(3) the frequency-domain Darcy's law for the frequency-dependent resistive friction,
(4) derivation of the time-domain Darcy's law for the frequency-dependent resistive friction using Laplace–Carson transform,
(5) numerical approximation of Darcy's law using an efficient optimization procedure,
(6) derivation of equations of motion for an averaged medium representing strongly heterogeneous medium with the frequency-dependent resistive friction,
(7) partitioning of the unifying equation into stiff and non-stiff systems,
(8) the FD scheme,
(9) numerical verification against the semi-analytical method,
(10) illustrative example for the low and high permeable sediments in a local surface basin.

We address the 2-D P-SV problem. The approach can be readily extended to the 3-D problem.

2 CONSTITUTIVE LAW

2.1 Smoothly heterogeneous isotropic poroelastic medium

The constitutive relations for the 2-D P-SV problem may be written as

$$
\begin{bmatrix}
\sigma_{xx} \\
\sigma_{zz} \\
\sigma_{xz} \\
-p
\end{bmatrix}
=
\begin{bmatrix}
\Lambda + \alpha^2 M & \lambda + \alpha^2 M & 0 & \alpha M \\
\lambda + \alpha^2 M & \Lambda + \alpha^2 M & 0 & \alpha M \\
0 & 0 & 2\mu & 0 \\
\alpha M & \alpha M & 0 & M
\end{bmatrix}
\begin{bmatrix}
\varepsilon_{xx} \\
\varepsilon_{zz} \\
\varepsilon_{xz} \\
\varepsilon_w
\end{bmatrix},
\tag{1}
$$

where σ_{ij} is the total stress component, p the fluid pressure, ε_{ij} the solid–matrix strain component, $\varepsilon_w \equiv w_{k,k} = w_{x,x} + w_{z,z}$, w_i displacement component of the fluid relative to the solid matrix, $\Lambda \equiv \lambda + 2\mu$, λ and μ Lamé elastic coefficients of the solid matrix, α poroelastic coefficient of effective stress and M is the solid–fluid coupling modulus.

The constitutive law does not include viscoelasticity of the solid matrix. We will address this aspect in a further work. The law, however, is valid for three models of the poroelastic medium with respect to attenuation in the fluid: (i) zero resistive friction, (ii) non-zero constant resistive friction and (iii) frequency-dependent resistive friction.

2.2 Boundary conditions at a material interface

At an interface between two poroelastic materials indicated by the $^+$ and $–$ superscripts, the boundary conditions require continuity of the (i) traction vector, (ii) fluid pressure, (iii) solid displacement vector and (iv) normal component of the displacement of the fluid relative to the solid matrix. The conditions may be written as

$$
\begin{aligned}
\sigma_{ij}^+ n_j &= \sigma_{ij}^- n_j \\
p^+ &= p^- \\
u_i^+ &= u_i^- \\
w_i^+ n_i &= w_i^- n_i,
\end{aligned}
\tag{2}
$$

where n_i is the component of the unit normal to the interface and u_i the solid displacement vector component. Einstein's summation convention for repeating indices is assumed.

2.3 Constitutive law for the averaged poroelastic medium

Moczo *et al.* (2019) developed a discrete representation of material heterogeneity including material interfaces. They demonstrated the subcell resolution that makes it possible to model an arbitrary shape and position of an interface in the grid. At the same time, the structure and thus the number of operations in the FD scheme is unchanged compared to that for the homogeneous or smoothly heterogeneous medium. The matrix form of the temporal derivatives of the constitutive relations for the averaged medium may be written as

$$
\begin{bmatrix}
\dfrac{\partial \sigma_{xx}}{\partial t} \\[2mm]
\dfrac{\partial \sigma_{zz}}{\partial t} \\[2mm]
\dfrac{\partial \sigma_{xz}}{\partial t} \\[2mm]
-\dfrac{\partial p}{\partial t}
\end{bmatrix}
=
\begin{bmatrix}
XX + \dfrac{XP\,XP}{\Psi} & XZ + \dfrac{XP\,ZP}{\Psi} & 0 & \dfrac{XP}{\Psi} \\[2mm]
XZ + \dfrac{XP\,ZP}{\Psi} & ZZ + \dfrac{ZP\,ZP}{\Psi} & 0 & \dfrac{ZP}{\Psi} \\[2mm]
0 & 0 & 2\langle\mu\rangle^{Hxz} & 0 \\[2mm]
\dfrac{XP}{\Psi} & \dfrac{ZP}{\Psi} & 0 & \dfrac{1}{\Psi}
\end{bmatrix}
\begin{bmatrix}
\dfrac{\partial v_x}{\partial x} \\[2mm]
\dfrac{\partial v_z}{\partial z} \\[2mm]
\dfrac{1}{2}\left(\dfrac{\partial v_x}{\partial z} + \dfrac{\partial v_z}{\partial x} \right) \\[2mm]
\dfrac{\partial q_x}{\partial x} + \dfrac{\partial q_z}{\partial z}
\end{bmatrix}.
\tag{3}
$$

Here $v_i = \partial u_i/\partial t$ is the particle-velocity component of the solid matrix, $q_i = \partial w_i/\partial t$ the particle-velocity component of fluid relative to the matrix and

$$
XX = \left\langle \left\langle \Lambda - \frac{\lambda^2}{\Lambda} \right\rangle^z + \left(\left\langle \frac{\lambda}{\Lambda} \right\rangle^z \right)^2 \langle \Lambda \rangle^{Hz} \right\rangle^{Hx}
$$

$$
ZZ = \left\langle \left\langle \Lambda - \frac{\lambda^2}{\Lambda} \right\rangle^x + \left(\left\langle \frac{\lambda}{\Lambda} \right\rangle^x \right)^2 \langle \Lambda \rangle^{Hx} \right\rangle^{Hz}
$$

$$
XZ = \left\langle \frac{\lambda}{\Lambda} \right\rangle^{xz} \langle \Lambda \rangle^{Hxz}
\tag{4}
$$

$$XP = \left\langle \left\langle \left\langle \Lambda - \frac{\alpha\,\lambda}{\Lambda} \right\rangle^z + \left\langle \frac{\alpha}{\Lambda} \right\rangle^z \left\langle \frac{\lambda}{\Lambda} \right\rangle^z \langle \Lambda \rangle^{Hz} \right\rangle^{Hx}\right.$$
$$\left.\left\langle \frac{\left\langle \alpha - \frac{\alpha\,\lambda}{\Lambda} \right\rangle^z + \left\langle \frac{\alpha}{\Lambda} \right\rangle^z \left\langle \frac{\lambda}{\Lambda} \right\rangle^z \langle \Lambda \rangle^{Hz}}{\left\langle \Lambda - \frac{\alpha\,\lambda}{\Lambda} \right\rangle^z + \left\langle \frac{\alpha}{\Lambda} \right\rangle^z \left\langle \frac{\lambda}{\Lambda} \right\rangle^z \langle \Lambda \rangle^{Hz}} \right\rangle^x \right\rangle \tag{5}$$

$$ZP = \left\langle \left\langle \left\langle \Lambda - \frac{\alpha\,\lambda}{\Lambda} \right\rangle^x + \left\langle \frac{\alpha}{\Lambda} \right\rangle^x \left\langle \frac{\lambda}{\Lambda} \right\rangle^x \langle \Lambda \rangle^{Hx} \right\rangle^{Hz}\right.$$
$$\left.\left\langle \frac{\left\langle \alpha - \frac{\alpha\,\lambda}{\Lambda} \right\rangle^x + \left\langle \frac{\alpha}{\Lambda} \right\rangle^x \left\langle \frac{\lambda}{\Lambda} \right\rangle^x \langle \Lambda \rangle^{Hx}}{\left\langle \Lambda - \frac{\alpha\,\lambda}{\Lambda} \right\rangle^x + \left\langle \frac{\alpha}{\Lambda} \right\rangle^x \left\langle \frac{\lambda}{\Lambda} \right\rangle^x \langle \Lambda \rangle^{Hx}} \right\rangle^z \right\rangle \tag{6}$$

$$\Psi = \left\langle \frac{1}{M} + \frac{\alpha^2}{\Lambda} \right\rangle^{xz} - \left(\left\langle \frac{\alpha}{\Lambda} \right\rangle^{xz} \right)^2 \langle \Lambda \rangle^{Hxz}. \tag{7}$$

Symbols $\langle \Phi \rangle^x$ and $\langle \Phi \rangle^{Hx}$, for example indicate arithmetic and harmonic averages of Φ, respectively, in the x-direction. The averaging applies to an area of grid cell $h \times h$ centred at a position of the corresponding stress component or fluid pressure. In case of a generally heterogeneous medium the averages are evaluated by a numerical integration.

Apart from the temporal derivative, relation (3) has the same form as relation (1) for the smoothly heterogeneous medium. Averaging of the field quantities is neglected. The stiffness matrices in relations (1) and (3) have the same number of 7 (considering the matrix symmetry) non-zero elements. The difference is in the number of independent elements. The matrix in (1) has 4 independent elements whereas the matrix in (3) has all 7 independent elements.

Note that the constitutive law is the same for both the Biot and JKD models of poroelastic medium.

3 EQUATIONS OF MOTION

3.1 Equations of motion for the poroelastic medium with a constant resistive friction

Equations may be written as

$$\begin{aligned} \rho\,\frac{\partial v_i}{\partial t} &= \frac{\partial \sigma_{ij}}{\partial x_j} &&-\rho_f\,\frac{\partial q_i}{\partial t} \\ m\,\frac{\partial q_i}{\partial t} &= -\frac{\partial p}{\partial x_i} &&-\rho_f\,\frac{\partial v_i}{\partial t} - b\,q_i, \end{aligned} \tag{8}$$

where $\rho = (1 - \phi)\,\rho_s + \phi\,\rho_f$ is the composite (or total) density, ρ_s and ρ_f are the solid and fluid densities, respectively, $m = T\rho_f/\phi$ is the mass coupling coefficient, T tortuosity, $b = \eta/\kappa_0$ resistive friction, η dynamic viscosity and κ_0 is the intrinsic (hydraulic) permeability.

The first of eq. (8) represents Biot–Euler dynamic equation. The first two terms are well known from the elastic continuum, the third term represents the relative motion of the fluid with respect to the solid matrix. The second equation is the dynamic Darcy's law in the low-frequency regime for the fluid flow in pores caused by the wave-induced pressure gradient in fluid and acceleration of the matrix. The flow of the viscous fluid is accompanied with friction between the fluid and matrix. The corresponding attenuation of motion is thus of kinetic nature and is represented in Darcy's law by the term with resistive friction $b = \eta/\kappa_0$. However, this term is well representing the attenuation at frequencies below the Biot's characteristic frequency

$$f_c = \frac{\eta\,\phi}{2\,\pi\,\rho_f\,T\,\kappa_0} = \frac{1}{2\pi}\,\frac{\phi}{T\,\rho_f}\,b. \tag{9}$$

Approximately, the Biot's frequency separates the so-called low-frequency (LF) and high-frequency (HF) regimes.

As, for example Masson *et al.* (2006) explain, the flow profile in each pore is at low frequencies controlled by viscous forces and is locally laminar (parabolic). At high frequencies, inertial effects begin to dominate and cause a turbulent flow except a thin layer near the solid where viscous forces remain dominant. In the case of an inviscid fluid, the turbulent flow would result in the ideal plug flow with constant velocity everywhere. The thickness of the boundary layer decreases with $1/\sqrt{\omega}$. Being frequency dependent, the fluid flow at HF regime cannot be properly described by Darcy's law with the constant resistive friction. A frequency-dependent resistive friction must be used.

3.2 Darcy's law for the poroelastic medium with the frequency-dependent permeability and resistive friction in the frequency domain

Assuming a harmonic $e^{\,i\,\omega\,t}$ time dependence, the generalized Darcy's law in the frequency domain may be written as

$$\frac{\eta}{\hat{\kappa}\,(\omega)}\,\hat{q}_i = -\frac{\partial\,\hat{p}}{\partial x_i} - i\,\omega\,\rho_f\,\hat{v}_i \tag{10}$$

with hat indicating the Fourier transform over time and $\hat{\kappa}(\omega)$ representing a frequency-dependent dynamic permeability. Johnson *et al.* (1987) incorporated both the LF and HF behaviours in one model (often called the JKD model according to Johnson, Koplik and Dashen) using the complex frequency-dependent dynamic permeability $\hat{\kappa}(\omega)$

$$\hat{\kappa}\,(\omega) = \kappa_0\left[\sqrt{1 + i\,\frac{\omega}{\Omega}} + i\,\frac{\omega}{\omega_c}\right]^{-1} \tag{11}$$

with auxiliary variable $\Omega = n_J\,\omega_c/4$, dimensionless parameter n_J and $\omega_c = 2\,\pi\,f_c$. Note that Johnson *et al.* (1987) do not use symbol n_j; they assume directly values 8 or 12. Also note that $\kappa_0 = \lim_{\omega\to 0}\hat{\kappa}(\omega)$. Denoting the JKD viscous operator,

$$\hat{F}^{\mathrm{JKD}}\,(\omega) \equiv \frac{1}{\sqrt{\Omega}}\sqrt{\Omega + i\,\omega}. \tag{12}$$

Darcy's law may be written as

$$i\,\omega\,m\,\hat{q}_i = -\frac{\partial\,\hat{p}}{\partial x_i} - i\,\omega\,\rho_f\,\hat{v}_i - \frac{\eta}{\kappa_0}\hat{F}^{JKD}\,\hat{q}_i. \tag{13}$$

Considering expansion of $\hat{F}^{JKD}(\omega)$

$$\hat{F}^{\mathrm{JKD}} \approx 1 + 2\,i\,\frac{\omega}{n_J\,\omega_c} + O\left(\frac{\omega^2}{\omega_c^2}\right) \tag{14}$$

and the LF regime, that is, $\omega/\omega_c << 1$, only the first term in the expansion applies and thus the LF approximation of the operator is

$$\hat{F}^{\mathrm{LF}}\,(\omega) \approx 1. \tag{15}$$

Consequently, Darcy's law in the LF regime simplifies to

$$i\,\omega\,m\,\hat{q}_i = -\frac{\partial\,\hat{p}}{\partial x_i} - i\,\omega\,\rho_f\,\hat{v}_i - b\,\hat{q}_i \tag{16}$$

which is the Darcy's law from eq. (8) in the frequency domain.

3.3 Darcy's law for the poroelastic medium with the frequency-dependent permeability and resistive friction in the time domain

Masson *et al.* (2006) presented the time-domain Darcy's law with reference to Plyushchenkov & Turchaninov (2000). Plyushchenkov & Turchaninov mentioned that they could have obtained the time-domain JKD operator using Laplace transform but they did not show the derivation itself. Blanc *et al.* (2012) and Blanc (2013) referred to Hanyga's (2001) concept of shifted fractional derivative. Because we were unable to derive the time-domain JKD operator using the shifted fractional derivative and have not found the derivation in the literature, we present here our derivation of the time-domain Darcy's law based on the Laplace–Carson transform. For the Laplace–Carson transform we refer to Ditkin & Prudnikov (1965). [We made our decision also based on discussions with experts in the field (Podlubný & Petráš 2020 personal communication), who questioned the concept of the shifted fractional derivative.]

The inverse Laplace–Carson transform of the JKD operator

The Laplace–Carson transform $\mathcal{LC}$ is defined as

$$\hat{f}\,(s) \equiv \mathcal{LC}\,\{f\,(t)\,;\,s\} = s\int_0^\infty f\,(t)\,e^{-s\,t}\mathrm{d}t = s\,L\,\{f\,(t)\,;\,s\}, \tag{17}$$

where s is the Laplace–Carson complex variable and $\mathcal{L}\{f(t);\,s\}$ is the Laplace transform. Ditkin & Prudnikov (1965) presented analytical relations for the forward and inverse Laplace–Carson transforms of variety of mathematical functions. According to their eq. (22.39)

$$\mathcal{LC}^{-1}\left\{\sqrt{a + s}\right\} = \frac{e^{-a\,t}}{\sqrt{\pi\,t}} + \sqrt{a}\,\mathrm{erf}\left(\sqrt{a\,t}\right), \tag{18}$$

where a is an arbitrary constant and erf the Error function

$$\mathrm{erf}\,(t) = \frac{2}{\sqrt{\pi}}\int_0^t e^{-u^2}\mathrm{d}u. \tag{19}$$

Substituting $i\,\omega$ in $\hat{F}^{JKD}(\omega)$, eq. (12), by s, we have

$$\hat{F}^{JKD}(\omega) = \frac{1}{\sqrt{\Omega}}\sqrt{\Omega + s}. \tag{20}$$

Using (18)

$$F^{\text{JKD}}(t) = \mathcal{LC}^{-1}\left\{\frac{1}{\sqrt{\Omega}}\sqrt{\Omega + s}\right\} = \frac{1}{\sqrt{\Omega}}\left[\frac{e^{-\Omega t}}{\sqrt{\pi\,t}} + \sqrt{\Omega}\,\,\text{erf}\left(\sqrt{\Omega\,t}\right)\right]. \tag{21}$$

Darcy's law in the time domain

Substituting $i\,\omega$ by s in eq. (13), considering '$\hat{a}$' an indication of the $\mathcal{LC}$ transform, applying the inverse $\mathcal{LC}$ transform to the equation and considering relation (e.g. Lemaitre & Chaboche 1990)

$$\mathcal{LC}^{-1}\left\{s\,\hat{f}(s)\right\} = \frac{d\,f(t)}{dt} \tag{22}$$

we obtain

$$m\,\frac{\partial q_i}{\partial t} = -\frac{\partial p}{\partial x_i} - \rho_f\,\frac{\partial v_i}{\partial t} - \frac{\eta}{\kappa_0}\mathcal{LC}^{-1}\left\{\hat{F}^{\text{JKD}}\,\hat{q}_i\right\}. \tag{23}$$

The last term in the equation may be rewritten as

$$\frac{\eta}{\kappa_0}\mathcal{LC}^{-1}\left\{\hat{F}^{\text{JKD}}\,\hat{q}_i\right\} = \frac{\eta}{\kappa_0}\left[F^{\text{JKD}} * dq_i\right] = \frac{\eta}{\kappa_0}\int_0^t F^{\text{JKD}}(t-\tau)\,\frac{\partial q_i(\tau)}{\partial\tau}\,d\tau. \tag{24}$$

Here we used the Stieltjes convolution relation (e.g. Bettina & Wilmanski 2014) for the Laplace–Carson transform

$$\mathcal{LC}^{-1}\left\{\hat{f}\cdot\hat{g}\right\} = f * dg. \tag{25}$$

Here dg denotes a differential of function g. Using (21) we rewrite the r.h.s. (right-hand side) of eq. (24):

$$\frac{\eta}{\kappa_0}\int_0^t F^{\text{JKD}}(t-\tau)\,\frac{\partial q_i(\tau)}{\partial\tau}\,d\tau = \frac{\eta}{\kappa_0\sqrt{\Omega}}\int_0^t\frac{e^{-\Omega(t-\tau)}}{\sqrt{\pi\,(t-\tau)}}\,\frac{\partial q_i(\tau)}{\partial\tau}\,d\tau + \frac{\eta}{\kappa_0}\int_0^t\text{erf}\left(\sqrt{\Omega\,(t-\tau)}\right)\frac{\partial q_i(\tau)}{\partial\tau}\,d\tau. \tag{26}$$

The second term on the r.h.s. may be rewritten using commutativity relation $f * dg = df * g$ and definition (19) as

$$\frac{\eta}{\kappa_0}\int_0^t\text{erf}\left(\sqrt{\Omega\,(t-\tau)}\right)\frac{\partial q_i(\tau)}{\partial\tau}\,d\tau = \frac{2}{\sqrt{\pi}}\frac{\eta}{\kappa_0}\int_0^t\left[\frac{d}{d\tau}\int_0^{\sqrt{\Omega\tau}}e^{-u^2}du\right]q_i(t-\tau)\,d\tau. \tag{27}$$

Using the Leibniz rule for differentiation the integral with respect to parameter inside the brackets on the r.h.s. of the latter equation we obtain

$$\frac{\eta}{\kappa_0}\int_0^t\text{erf}\left(\sqrt{\Omega\,(t-\tau)}\right)\frac{\partial q_i(\tau)}{\partial\tau}\,d\tau = \frac{\eta}{\kappa_0}\frac{1}{\sqrt{\Omega}}\int_0^t\frac{e^{-\Omega\tau}}{\sqrt{\pi\,\tau}}\,\Omega\,q_i(t-\tau)\,d\tau. \tag{28}$$

Next, we first substitute τ by $t-\gamma$ and then γ by τ:

$$\frac{\eta}{\kappa_0}\int_0^t\text{erf}\left(\sqrt{\Omega\,\tau}\right)\frac{\partial q_i(t-\tau)}{\partial\tau}\,d\tau = \frac{\eta}{\kappa_0}\frac{1}{\sqrt{\Omega}}\int_0^t\frac{e^{-\Omega(t-\tau)}}{\sqrt{\pi\,(t-\tau)}}\,\Omega\,q_i(\tau)\,d\tau. \tag{29}$$

Substituting the second term on the r.h.s. of eq. (26) by the r.h.s. of eq. (29), and recalling eq. (24) we have

$$\frac{\eta}{\kappa_0}\mathcal{LC}^{-1}\left\{\hat{F}^{\text{JKD}}\,\hat{q}_i\right\} = \frac{\eta}{\kappa_0}\frac{1}{\sqrt{\Omega}}\left[\int_0^t\frac{e^{-\Omega(t-\tau)}}{\sqrt{\pi\,(t-\tau)}}\,\frac{\partial q_i(\tau)}{\partial\tau}\,d\tau + \int_0^t\frac{e^{-\Omega(t-\tau)}}{\sqrt{\pi\,(t-\tau)}}\,\Omega\,q_i(\tau)\,d\tau\right]. \tag{30}$$

We obtain the Darcy's law in the time domain as

$$m\,\frac{\partial q_i}{\partial t} = -\frac{\partial p}{\partial x_i} - \rho_f\,\frac{\partial v_i}{\partial t} - \frac{\eta}{\kappa_0}\frac{1}{\sqrt{\Omega}}\int_0^t\frac{e^{-\Omega(t-\tau)}}{\sqrt{\pi\,(t-\tau)}}\left[\frac{\partial q_i(\tau)}{\partial\tau} + \Omega\,q_i(\tau)\right]d\tau. \tag{31}$$

which has the same form as the Darcy's law presented without demonstration by Masson & Pride (2010).

3.4 Approximation of Darcy's law in the time domain

The convolution in the Darcy's law involves the entire history of $q_i(t)$ and thus poses tremendous memory requirements in a direct numerical implementation. Aiming to avoid the convolution by replacing it using memory variables, term $1/\sqrt{t-\tau}$ poses a serious problem. This is because desired memory variables must obey ordinary differential equations. Such equations are obtained by differentiating the convolution term (here the term in eq. 31) with respect to time t. However, due to $1/\sqrt{t-\tau}$, the Leibniz rule for differentiation of an integral with respect

to parameter cannot be applied. Blanc *et al.* (2012) and Blanc (2013) replaced the term using the diffusive representation based on Euler's Γ function

$$\frac{1}{\sqrt{t}} = \frac{1}{\sqrt{\pi}} \int_0^\infty \frac{1}{\sqrt{\theta}} \, e^{-\theta t} \mathrm{d}\theta \tag{32}$$

Note that relation (32) can be easily derived from the standard form of Γ function. Using relation (32), the convolution term in eq. (31) may be written as

$$\frac{\eta}{\kappa_0} \frac{1}{\sqrt{\Omega}} \frac{1}{\pi} \int_0^\infty \frac{1}{\sqrt{\theta}} \left\{ \int_0^t e^{-\theta(t-\tau)} e^{-\Omega(t-\tau)} \left[\frac{\partial q_i(\tau)}{\partial \tau} + \Omega \, q_i(\tau) \right] \mathrm{d}\tau \right\} \mathrm{d}\theta$$
$$= \frac{\eta}{\kappa_0} \frac{1}{\sqrt{\Omega}} \frac{1}{\pi} \int_0^\infty \frac{1}{\sqrt{\theta}} \psi^i(\theta, t) \, \mathrm{d}\theta \tag{33}$$

where

$$\psi^i(\theta, \, t) = \int_0^t e^{-(\theta+\Omega)(t-\tau)} \left[\frac{\partial q_i(\tau)}{\partial \tau} + \Omega \, q_i(\tau) \right] \mathrm{d}\tau. \tag{34}$$

is the diffusive memory variable satisfying

$$\frac{\partial \psi^i}{\partial t} = -(\theta + \Omega) \, \psi^i + \frac{\partial q_i}{\partial t} + \Omega \, q_i \quad ; \quad \psi(\theta, 0) = 0. \tag{35}$$

The improper integral in eq. (33) multiplied by $1/\pi$ can be approximated using N points with weights a_l and abscissae θ_l:

$$\frac{\eta}{\kappa_0} \frac{1}{\sqrt{\Omega}} \frac{1}{\pi} \int_0^\infty \frac{1}{\sqrt{\theta}} \, \psi^i(\theta, \, t) \mathrm{d}\theta \approx \frac{\eta}{\kappa_0} \frac{1}{\sqrt{\Omega}} \sum_{l=1}^N a_l \, \psi^i(t, \, \theta_l) \equiv \frac{\eta}{\kappa_0} \frac{1}{\sqrt{\Omega}} \sum_{l=1}^N a_l \, \psi_l^i(t). \tag{36}$$

Consequently, the diffusive approximation of the Darcy's law may be written as

$$m \frac{\partial q_i}{\partial t} = -\frac{\partial p}{\partial x_i} - \rho_f \frac{\partial v_i}{\partial t} - \frac{\eta}{\kappa_0} \frac{1}{\sqrt{\Omega}} \sum_{l=1}^N a_l \, \psi_l^i(t) \tag{37}$$

with

$$\frac{\partial \psi_l^i}{\partial t} = -(\theta_l + \Omega) \, \psi_l^i + \frac{\partial q_i}{\partial t} + \Omega \, q_i \quad ; \quad l = 1, \dots, N. \tag{38}$$

Weights a_l and abscissae θ_l have to be determined.

The exact Darcy's law (31) and its approximation (37) may be written using the exact (F^{JKD}) and approximate (F^{DA}) operators:

$$m \frac{\partial q_i}{\partial t} = -\frac{\partial p}{\partial x_i} - \rho_f \frac{\partial v_i}{\partial t} - \frac{\eta}{\kappa_0} F^{\mathrm{JKD}}(t) * q_i(t) \tag{39}$$

$$m \frac{\partial q_i}{\partial t} = -\frac{\partial p}{\partial x_i} - \rho_f \frac{\partial v_i}{\partial t} - \frac{\eta}{\kappa_0} F^{\mathrm{DA}}(t) * q_i(t). \tag{40}$$

$\hat{F}^{\mathrm{JKD}}(\omega)$ is given by eqs (12) and (20). For $\hat{F}^{DA}(\omega)$ we obtain, using Fourier-transformed eqs (40), (38) and (37),

$$\hat{F}^{\mathrm{DA}}(\omega) = \frac{\Omega + \mathrm{i}\,\omega}{\sqrt{\Omega}} \sum_{l=1}^N \frac{a_l}{\theta_l + \Omega + \mathrm{i}\,\omega}. \tag{41}$$
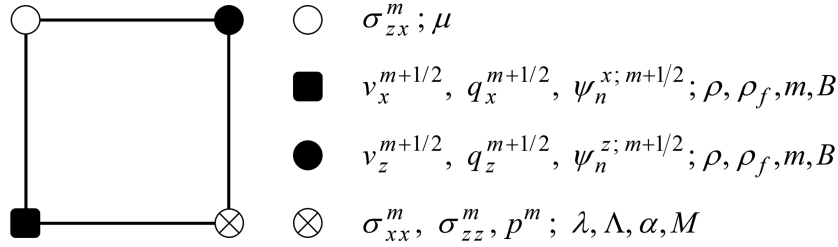
The relative error of $\hat{F}^{DA}(\omega)$ is

$$\left| \frac{\hat{F}^{\mathrm{DA}}(\omega)}{\hat{F}^{\mathrm{JKD}}(\omega)} - 1 \right| = \left| \sum_{l=1}^N a_l \frac{(\Omega + \mathrm{i}\,\omega)^{1/2}}{\theta_l + \Omega + \mathrm{i}\,\omega} - 1 \right| \tag{42}$$

Blanc (2013) examined five methods for determining a_l and θ_l in order to minimize the error, and found the non-linear constrained optimization the best approach.

Let $[\omega_{\min}, \omega_{\max}]$ be the frequency range of interest. Consider K frequencies $\tilde{\omega}_k$ distributed equidistantly on a logarithmic scale:

$$\begin{aligned} \tilde{\omega}_1 &= \sqrt{\omega_{\min} \, \omega_{\max}} \qquad \text{if } K = 1 \\ \tilde{\omega}_k &= \omega_{\min} \left(\frac{\omega_{\max}}{\omega_{\min}} \right)^{\frac{k-1}{K-1}}. \end{aligned} \tag{43}$$

Figure 1. Positions of the field variables (discrete approximations of the true variables in the continuum) and material parameters. For brevity, we indicate the material parameters as they appear in the equations for the smoothly heterogeneous medium.

Now we depart from Blanc *et al.* (2012) and Blanc (2013) in order to define an objective function based on the approach by Kristek *et al.* (2019). In principle, Ω may vary point-to-point. We want to avoid choosing an objective function which would lead to different values of weights a_l and abscissae θ_l for different values of Ω. It is computationally significantly more efficient to determine the same θ_l for the whole computational domain. Therefore, we define the objective function

$$\chi\left(\theta'_l, a_l'^{\,\Omega_1}, a_l'^{\,\Omega_2}\right) = \sqrt{\sum_{k=1}^{K}\left|\sum_{l=1}^{N}\left(a_l'^{\,\Omega_1}\right)^2 \frac{(\Omega_1 + i\,\tilde{\omega}_k)^{1/2}}{(\theta'_l)^2 + \Omega_1 + i\,\tilde{\omega}_k} - 1\right|^2 + \sum_{k=1}^{K}\left|\sum_{l=1}^{N}\left(a_l'^{\,\Omega_2}\right)^2 \frac{(\Omega_2 + i\,\tilde{\omega}_k)^{1/2}}{(\theta'_l)^2 + \Omega_2 + i\,\tilde{\omega}_k} - 1\right|^2}, \quad (44)$$

where Ω_1 and Ω_2 are the most differing values of Ω in the model, and

$$\left(\theta'_l\right)^2 = \theta_l, \quad \left(a'_l\right)^2 = a_l \quad (45)$$

are used in order to have θ_l and a_l positive, and to ensure the well-posedness of the approximation. Application of the Shor's r-algorithm (Kappel & Kuntsevich 2000) to the objective function yields values of θ'_l, $a_l'^{\,\Omega_1}$, $a_l'^{\,\Omega_2}$; $l = 1, ..., N$. Using the determined abscissae, we could use the Shor's r-algorithm for finding weights for other values of Ω in the model. We checked, however, that we would obtain weights very close to those that we can obtain more efficiently, using the determined abscissae, by the least-square optimization of the objective function

$$\chi^2(a_l) = \sum_{k=1}^{K}\left|\sum_{l=1}^{N} a_l \frac{(\Omega + i\,\tilde{\omega}_k)^{1/2}}{\theta_l + \Omega + i\,\tilde{\omega}_k} - 1\right|^2. \quad (46)$$

Further details on determination of θ_l and a_l can be found in Blanc (2013) and Gregor (2020).

3.5 Equations of motion for the averaged poroelastic medium

Both systems of equations of motion, for medium with constant resistive friction and medium with frequency-dependent permeability and resistive friction, may be written in the unified form as

$$\begin{aligned}
\rho\,\frac{\partial v_x}{\partial t} &= \frac{\partial \sigma_{xx}}{\partial x} + \frac{\partial \sigma_{xz}}{\partial z} - \rho_f\,\frac{\partial q_x}{\partial t} \\
\rho\,\frac{\partial v_z}{\partial t} &= \frac{\partial \sigma_{xz}}{\partial x} + \frac{\partial \sigma_{zz}}{\partial z} - \rho_f\,\frac{\partial q_z}{\partial t} \\
m\,\frac{\partial q_x}{\partial t} &= -\frac{\partial p}{\partial x} - \rho_f\,\frac{\partial v_x}{\partial t} - B\,P_x \\
m\,\frac{\partial q_z}{\partial t} &= -\frac{\partial p}{\partial z} - \rho_f\,\frac{\partial v_z}{\partial t} - B\,P_z
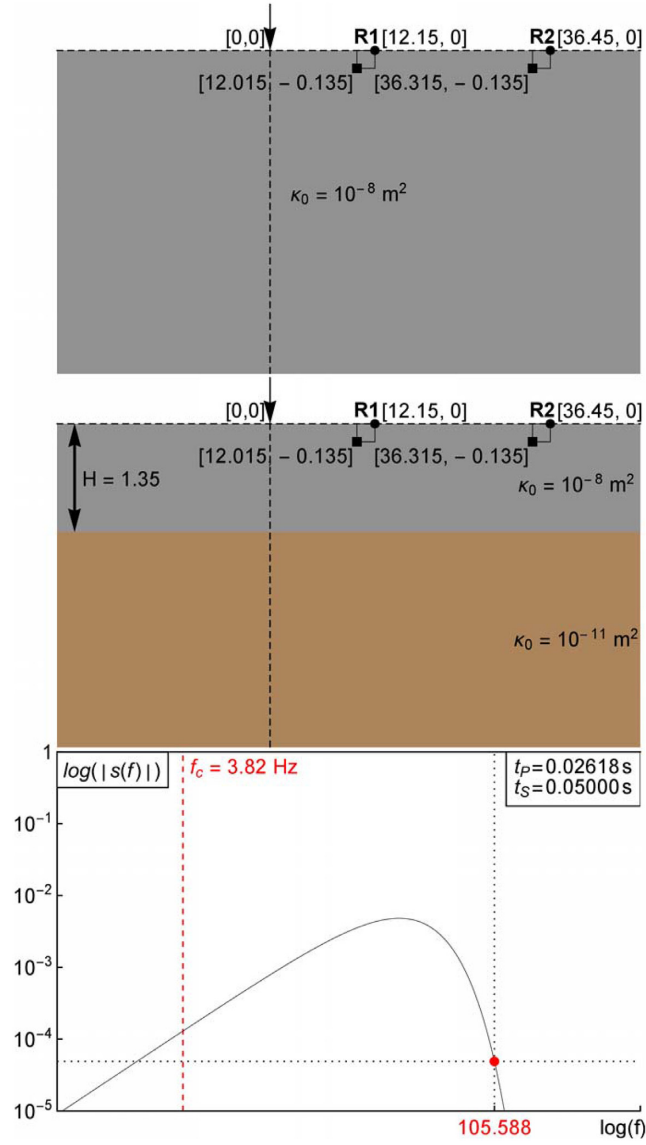\end{aligned} \quad (47)$$

where

$$B \equiv \frac{\eta}{\kappa_0}, \quad P_i \equiv q_i \quad (48)$$

in case of the constant resistive friction,

and

$$B \equiv \frac{\eta}{\kappa_0}\frac{1}{\sqrt{\Omega}}, \quad P_i \equiv \sum_{l=1}^{N} a_l\,\psi_l^i(t) \quad (49)$$

in case of the frequency-dependent permeability and resistive friction.

Figure 2. Upper panel: Source–receiver configuration in the model of a homogeneous half-space. Middle panel: Source–receiver configuration in the model of a layer over half-space. Bottom panel: Log–log spectrum of the Ricker signal and indication of the Biot's characteristic frequency.

Equations for the averaged medium can be derived in a similar way as in Moczo *et al.* (2019). In the matrix form:

$$
\begin{bmatrix}
\dfrac{\partial v_x}{\partial t} \\[2mm]
-\dfrac{\partial q_x}{\partial t} \\[2mm]
\dfrac{\partial v_z}{\partial t} \\[2mm]
-\dfrac{\partial q_z}{\partial t}
\end{bmatrix}
= \mathbf{M}(x,z)
\begin{bmatrix}
\dfrac{\partial \sigma_{xx}}{\partial x} + \dfrac{\partial \sigma_{xz}}{\partial z} \\[2mm]
\dfrac{\partial p}{\partial x} \\[2mm]
P_x \\[2mm]
\dfrac{\partial \sigma_{zz}}{\partial z} + \dfrac{\partial \sigma_{xz}}{\partial x} \\[2mm]
\dfrac{\partial p}{\partial z} \\[2mm]
P_z
\end{bmatrix}
\tag{50}
$$

Symbol	Units	Porous rock	Coarse sand
solid phase			
ρ_s	kg/m^3	2650	2650
K_s	Pa	$36\cdot 10^9$	$36\cdot 10^9$
fluid phase			
ρ_f	kg/m^3	1000	1000
K_f	Pa	$2.37\cdot 10^9$	$2.37\cdot 10^9$
η	$Pa\,s$	$1\cdot 10^{-3}$	$1\cdot 10^{-3}$
solid matrix (drained)			
K_m	Pa	$2.66068\cdot 10^9$	$2.66068\cdot 10^8$
μ	Pa	$1\cdot 10^9$	$1\cdot 10^8$
λ_m	Pa	$1.66068\cdot 10^9$	$1.66068\cdot 10^8$
ϕ		0.3	0.3
T		1.25	1.25
κ_0	m^2	$1\cdot 10^{-11}$	$1\cdot 10^{-8}$
saturated porous medium (undrained)			
λ_c	Pa	$3.0277\cdot 10^8$	$5.9723\cdot 10^8$
f_c	Hz	3819.72	3.82
n_J		8	8
velocities			
VP_{fast}^{inf}	m/s	2143	1945
VP_{slow}^{inf}	m/s	833	288
VS^{inf}	m/s	723	229

Figure 3. Material parameters.

Here

$$\mathbf{M}(x,z) = \begin{bmatrix} \dfrac{\langle F^x\rangle^z}{\langle S^x\rangle^z} & \dfrac{\langle G^x\rangle^z}{\langle S^x\rangle^z} & \dfrac{\langle H^x\rangle^z}{\langle S^x\rangle^z} & 0 & 0 & 0 \\[2ex] \dfrac{\langle R^x\rangle^z\left\langle \dfrac{G^x}{R^x}\right\rangle^z}{\langle S^x\rangle^z} & \dfrac{\langle P^x\rangle^z\langle G^x\rangle^z}{\langle S^x\rangle^z} & \dfrac{\langle P^x\rangle^z\langle H^x\rangle^z}{\langle S^x\rangle^z} & 0 & 0 & 0 \\[2ex] 0 & 0 & 0 & \dfrac{\langle F^z\rangle^x}{\langle S^z\rangle^x} & \dfrac{\langle G^z\rangle^x}{\langle S^z\rangle^x} & \dfrac{\langle H^z\rangle^x}{\langle S^z\rangle^x} \\[2ex] 0 & 0 & 0 & \dfrac{\langle R^z\rangle^x\left\langle \dfrac{G^z}{R^z}\right\rangle^x}{\langle S^z\rangle^x} & \dfrac{\langle P^z\rangle^x\langle G^z\rangle^x}{\langle S^z\rangle^x} & \dfrac{\langle P^z\rangle^x\langle H^z\rangle^x}{\langle S^z\rangle^x} \end{bmatrix} \tag{51}$$
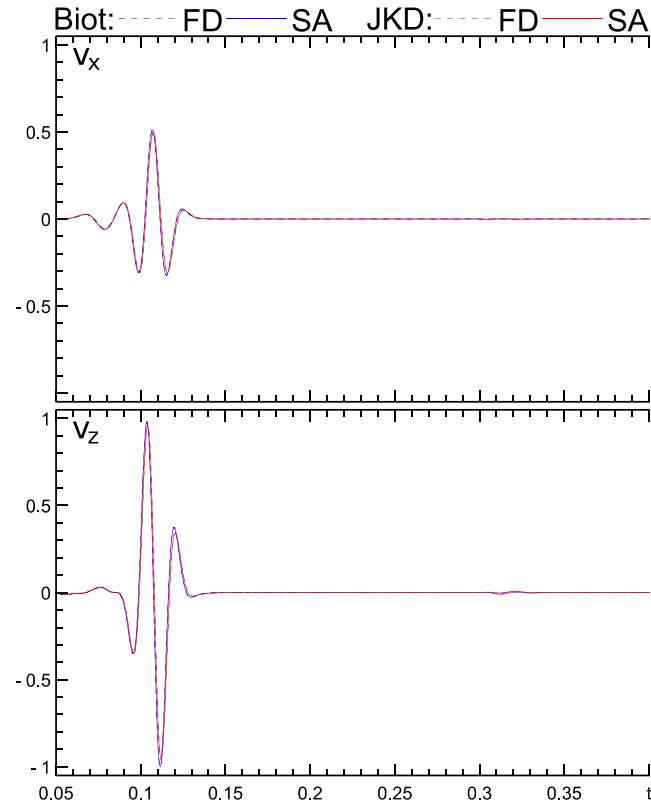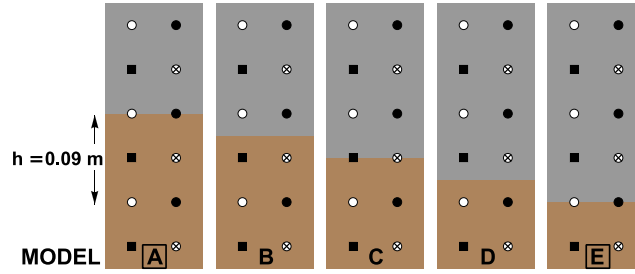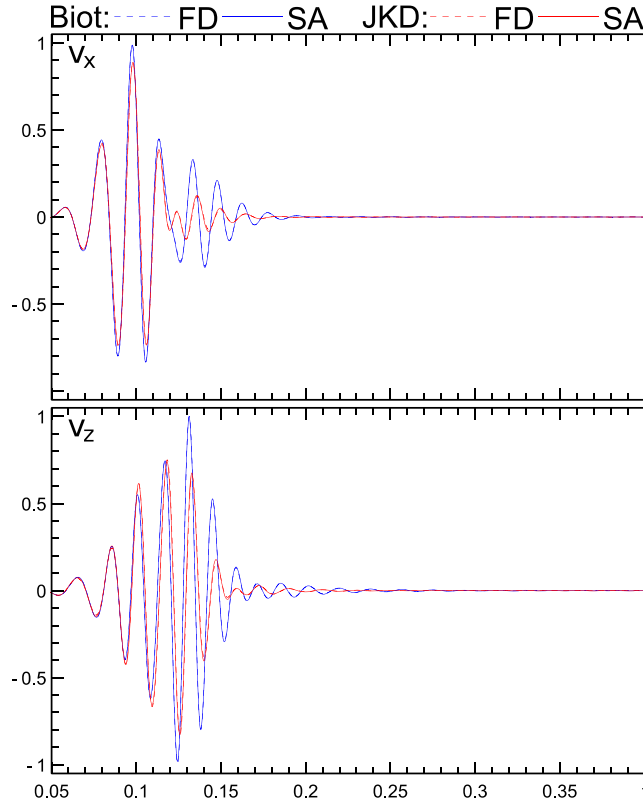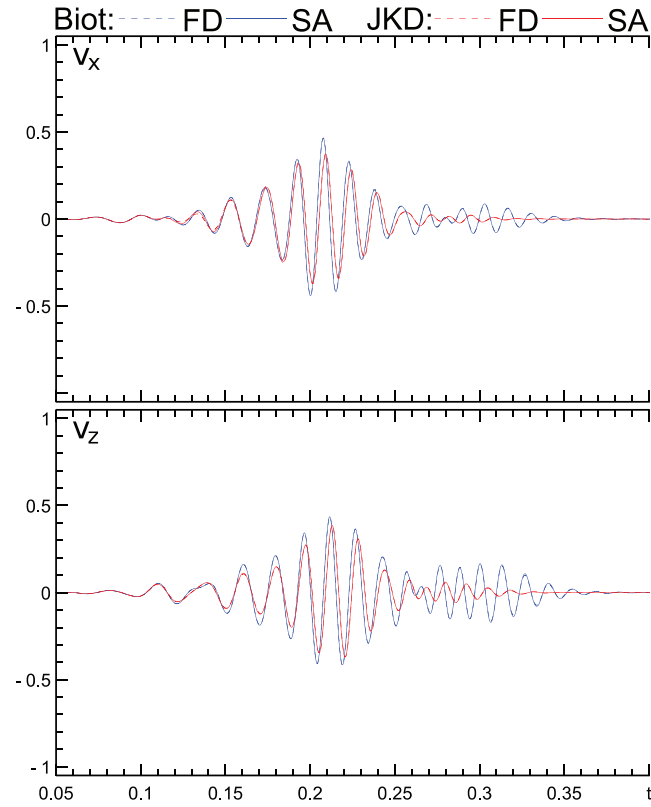
Figure 4. The v_x and v_z seismograms at receiver R1 in the model of the homogeneous half-space for the Biot's and JKD models calculated by the FD scheme and semi-analytical (SA) method.
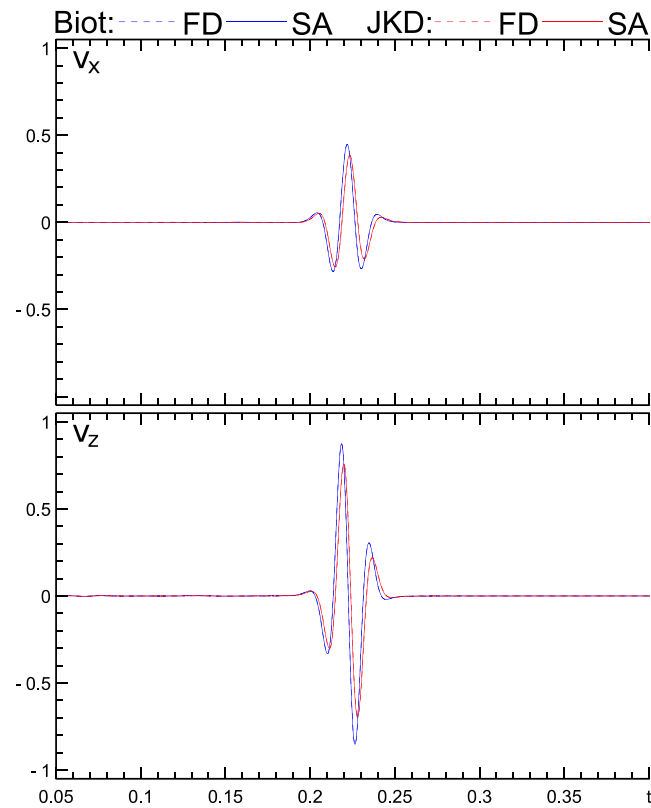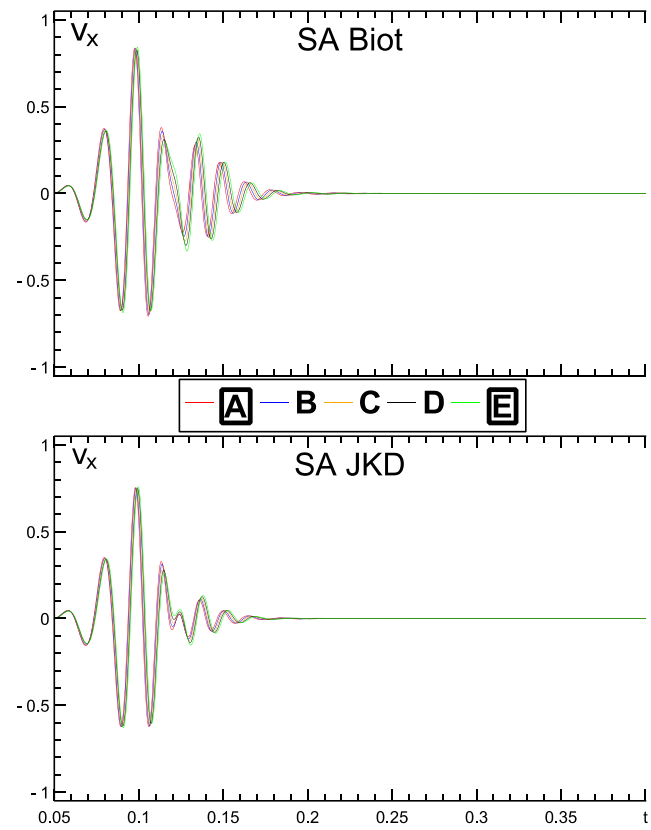

Figure 5. The same as in Fig. 4 but for receiver R2.

Figure 6. Five models differing by thickness of the layer – five positions of the horizontal layer-half-space interface in the same grid, labelled A, B, C, D and E. Labels A and E are framed in order to indicate that the distance between the two positions is just one grid spacing h. The source and receivers are at the same positions in the grid in all five cases.

Figure 7. The v_x and v_z seismograms at receiver R1 in the model of the layer over half-space for the Biot's and JKD models calculated by our FD scheme and semi-analytical (SA) method.

and

$$F^\xi \equiv \frac{1}{\langle \rho_f \rangle^\xi} \quad G^\xi \equiv \frac{1}{\langle m \rangle^\xi} \quad H^\xi \equiv \frac{\langle B \rangle^\xi}{\langle m \rangle^\xi}$$

$$P^\xi \equiv \frac{\langle \rho \rangle^\xi}{\langle \rho_f \rangle^\xi} \quad Q^\xi \equiv \frac{\langle \rho_f \rangle^\xi}{\langle m \rangle^\xi} \quad R^\xi \equiv \left\langle \frac{1}{\rho_f} \right\rangle^\xi \tag{52}$$

$$S^\xi \equiv P^\xi - Q^\xi$$

The averaging applies to an area of grid cell $h \times h$ centred at a position of the corresponding particle-velocity component. In case of a generally heterogeneous medium, the averages are evaluated by a numerical integration. Averaging of the field quantities is neglected. Note that eq. (47) for the smoothly heterogeneous medium could be written in the same matrix form as eq. (50)—in analogy with the constitutive relations for the smoothly heterogeneous medium and averaged medium.
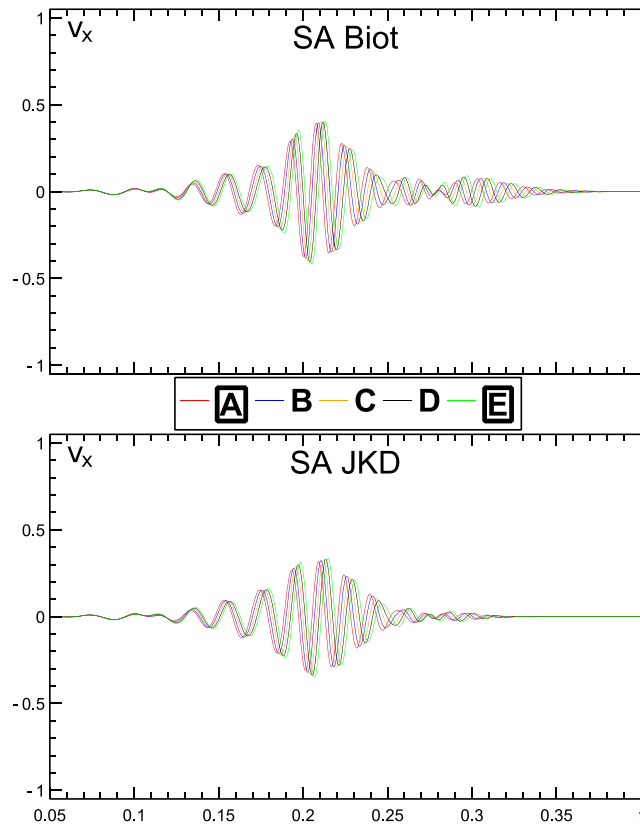
**Figure 8.** The same as in Fig. 7 but for receiver R2.

Figure 9. The v_x seismograms at receiver R1 in the five models with A–E thicknesses of the layer for the Biot's and JKD model variants calculated by the semi-analytical (SA) method.
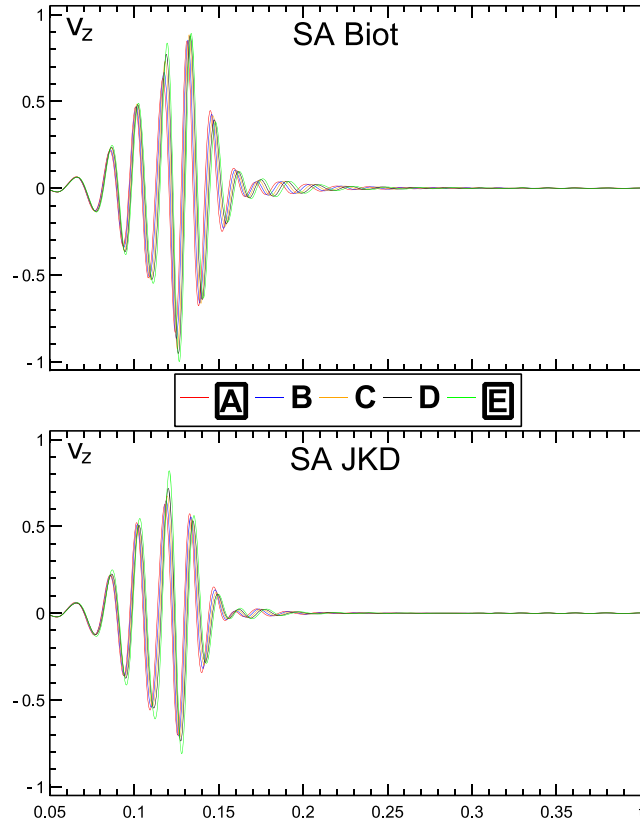
Figure 10. The same as in Fig. 9 but for the v_z seismograms.

Figure 11. The v_x seismograms at receiver R2 in the 5 models with A–E thicknesses of the layer for the Biot's and JKD model variants calculated by the semi-analytical (SA) method.
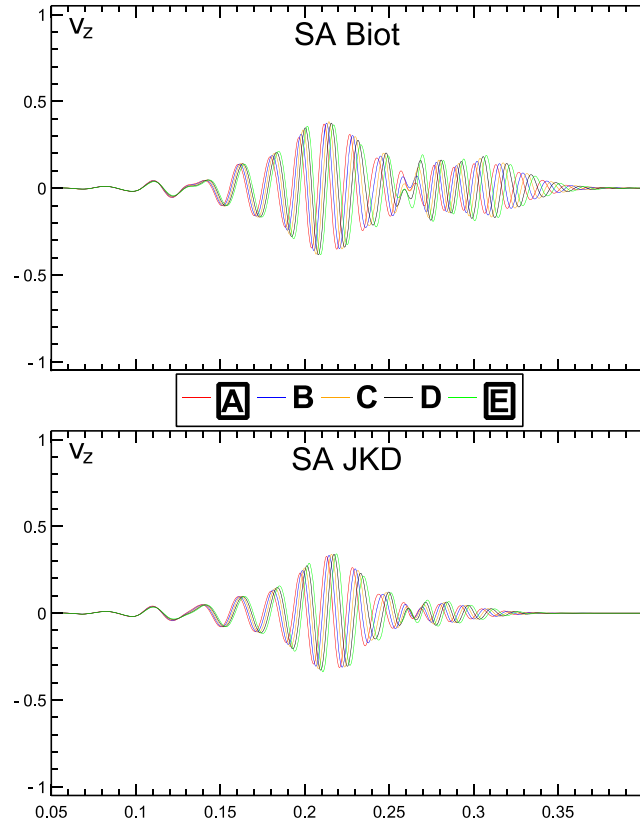
Figure 12. The same as in Fig. 11 but for the v_z seismograms.

For the averaged JKD medium we have to rewrite correspondingly the additional equations for the diffusive memory variables (38). We replace term $\partial q_i / \partial t$ by the r.h.s. of the corresponding equation for the averaged medium (50) and replace Ω by $\bar\Omega$:

$$\frac{\partial \psi_n^x}{\partial t} = -\left(\theta_n + \bar\Omega\right) \psi_n^x - \frac{\langle P^x\rangle^z \langle H^x\rangle^z}{\langle S^x\rangle^z} \sum_{l=1}^{N} a_l \, \psi_l^x - \frac{\langle R^x\rangle^z \left\langle \frac{G^x}{R^x}\right\rangle^z}{\langle S^x\rangle^z} \left(\frac{\partial \sigma_{xx}}{\partial x} + \frac{\partial \sigma_{xz}}{\partial z}\right) - \frac{\langle P^x\rangle^z \langle G^x\rangle^z}{\langle S^x\rangle^z} \frac{\partial p}{\partial x} + \bar\Omega \, q_x \tag{53}$$

and

$$\frac{\partial \psi_n^z}{\partial t} = -\left(\theta_n + \bar\Omega\right) \psi_n^z - \frac{\langle P^z\rangle^x \langle H^z\rangle^x}{\langle S^z\rangle^x} \sum_{l=1}^{N} a_l \, \psi_l^z - \frac{\langle R^z\rangle^x \left\langle \frac{G^z}{R^z}\right\rangle^x}{\langle S^z\rangle^x} \left(\frac{\partial \sigma_{xz}}{\partial x} + \frac{\partial \sigma_{zz}}{\partial z}\right) - \frac{\langle P^z\rangle^x \langle G^z\rangle^x}{\langle S^z\rangle^x} \frac{\partial p}{\partial z} + \bar\Omega \, q_z \tag{54}$$

with $n = 1, \ldots, N$ and

$$\bar\Omega \equiv \left(\frac{n_J}{4}\right)^2 \left\{ \frac{1}{2} \left[\langle H^x\rangle^z + \langle H^z\rangle^x\right] \right\}^2 \tag{55}$$

With reference to (52), we defined $\bar\Omega$ by the r.h.s. of eq. (55) because in the smoothly heterogeneous medium

$$\Omega = \left(\frac{n_J}{4}\right)^2 \left(\frac{B}{m}\right)^2 \tag{56}$$

with B given by eq. (49).

4 THE UNIFYING MATRIX-FORM EQUATION AND ITS PARTITIONING INTO STIFF AND NON-STIFF SYSTEMS

Constitutive relations (3), equations of motion (50) and additional equations for diffusive memory variables (53) and (54) for the averaged medium may be incorporated in the matrix-form equation

$$\frac{\partial \vec{Q}_q}{\partial t} + A_{qp} \frac{\partial \vec{Q}_p}{\partial x} + C_{qp} \frac{\partial \vec{Q}_p}{\partial z} = -S_{qp} \, \vec{Q}_p, \tag{57}$$
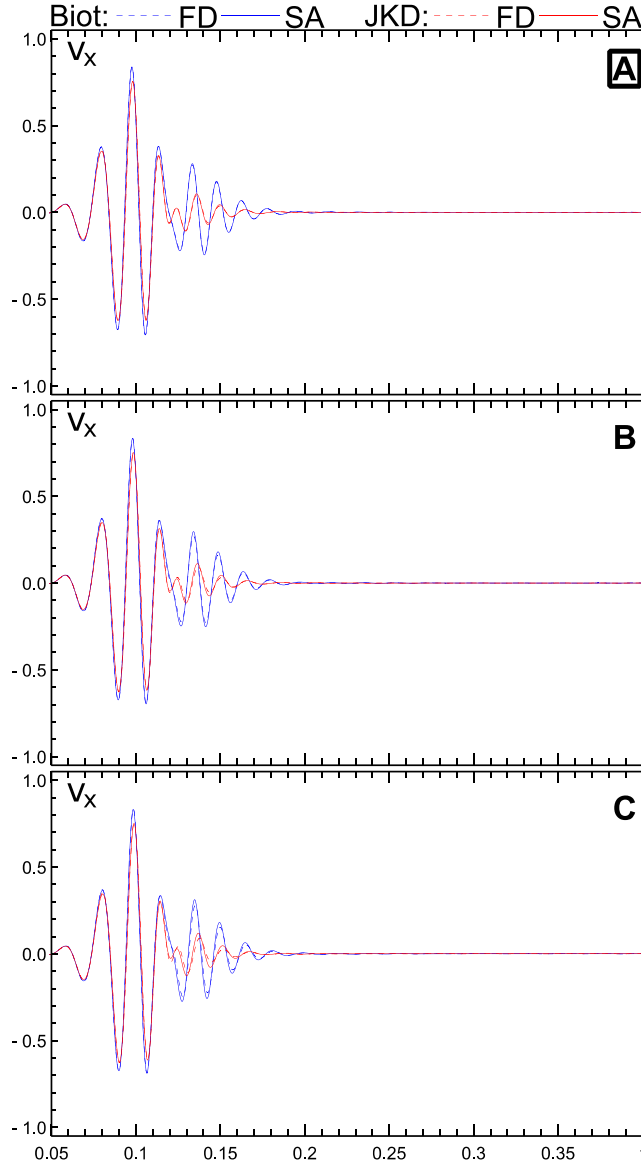
Figure 13. The v_x seismograms at receiver R1 in the models of the layer over half-space for the Biot's and JKD models calculated by the FD scheme and semi-analytical (SA) method. Labels A, B and C indicate the layer thicknesses and thus also positions of the layer-half-space interface in the FD grid (the grid being one and the same for all thicknesses/interface positions, see Fig. 6).

where $\vec{Q}_p$ is the vector with $p = 2N + 8$ elements

$$\vec{Q}_p \equiv \left(v_x, q_x, \psi_1^x, \ldots, \psi_N^x, v_z, q_z, \psi_1^z, \ldots, \psi_N^z, \sigma_{xx}, \sigma_{xz}, \sigma_{zz}, p \right)^T. \tag{58}$$

Matrices A_{qp}, C_{qp} and S_{qp} are relatively cumbersome. Therefore, they are specified in Appendix A. Blanc (2013) showed that $N = 3$ is sufficient. It is, however, recommended to evaluate the relative error (42) in order to check the level of approximation and choose possibly a higher value of N.

It is relatively simple to construct an explicit FD scheme with 4th-order accurate approximations of spatial derivatives and 2nd-order accurate approximations of the temporal derivatives on the staggered space–time grid if the resistive friction is zero ($b = 0$). If the friction is non-zero, constant or frequency dependent, such scheme requires a very small time step and thus becomes computationally inefficient. In order to overcome this complication, Carcione & Quiroga-Goode (1995) suggested to partition equations of motion into stiff and non-stiff equations. We applied the partitioning in our previous paper (Moczo *et al.* 2019) on poroelastic medium with constant resistive friction. Here we briefly outline a procedure similar to that by Blanc (2013). The difference comes from two aspects: (i) averaged material parameters and (ii) the same abscissae for the whole model.

Equation (57) may be partitioned into the non-stiff system

$$\frac{\partial \vec{Q}_q}{\partial t} + A_{qp} \frac{\partial \vec{Q}_p}{\partial x} + C_{qp} \frac{\partial \vec{Q}_p}{\partial z} = 0 \tag{59}$$
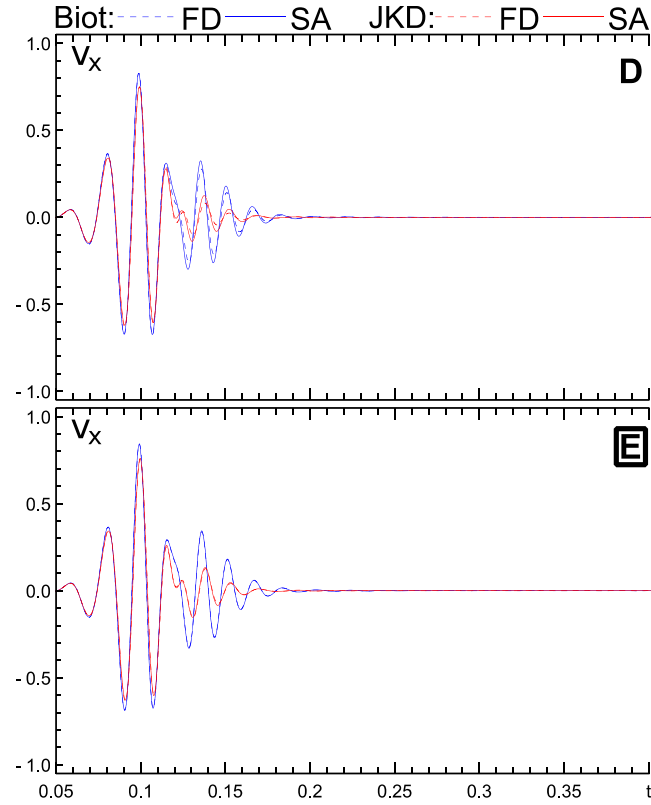
Figure 14. The same as in Fig. 13 but for the layer thicknesses/interface positions D and E.

and stiff system

$$\frac{\partial \vec{Q}_p}{\partial t} = -S_{qp}\,\vec{Q}_p \tag{60}$$

Using notation

$$
\begin{aligned}
^x\vec{Q} &\equiv \left(v_x, q_x, , \psi_1^x, \ldots, \psi_N^x\right)^T \\
^z\vec{Q} &\equiv \left(v_z, q_z, , \psi_1^z, \ldots, \psi_N^z\right)^T
\end{aligned}
\tag{61}
$$

and definition (84) (Appendix A), the stiff system (60) may be written as

$$
\frac{\partial}{\partial t}
\begin{pmatrix}
^x\vec{Q} \\
^z\vec{Q} \\
\sigma_{xx} \\
\sigma_{xz} \\
\sigma_{zz} \\
p
\end{pmatrix}
=
\begin{pmatrix}
S_{N+2,\,N+2}^x & 0_{N+2,\,N+2} & 0_{N+2,\,4} \\
0_{N+2,\,N+2} & S_{N+2,\,N+2}^z & 0_{N+2,\,4} \\
0_{\ \ 4,\,N+2} & 0_{\ \ 4,\,N+2} & 0_{\ \ 4,\,4}
\end{pmatrix}
\begin{pmatrix}
^x\vec{Q} \\
^z\vec{Q} \\
\sigma_{xx} \\
\sigma_{xz} \\
\sigma_{zz} \\
p
\end{pmatrix}
\tag{62}
$$

Matrices $S_{N+2,\,N+2}^x$ and $S_{N+2,\,N+2}^z$ do not depend on time. Therefore, the stiff system (62) can be solved analytically for $^x\vec{Q}$ and $^z\vec{Q}$:

$$
\begin{aligned}
^x\vec{Q}^*\Big|^{m+1/2} &= \exp\left(-\,S^x\,\Delta\right)\ {^x\vec{Q}}\Big|^{m-1/2} \\
^z\vec{Q}^*\Big|^{m+1/2} &= \exp\left(-\,S^z\,\Delta\right)\ {^z\vec{Q}}\Big|^{m-1/2}
\end{aligned}
\tag{63}
$$

Here, '∗' indicates analytical solution and the vertical bar '|' is used to indicate the time level. The matrix exponentials $\exp\left(-\,S^x\,\Delta\right)$ and $\exp\left(-\,S^z\,\Delta\right)$ can be computed by, for example the 'ExpoRkit' Fortran package (Hansen 2018) based on the scaling and squaring algorithm with the Padé approximation. The resulting matrix for $\exp\left(-\,S^x\,\Delta\right)$ is

$$
\exp\left(-\,S^x\,\Delta\right) \approx \tilde{S}^x =
\begin{pmatrix}
\tilde{s}_{v_x}^{v_x} & \tilde{s}_{v_x}^{q_x} & \tilde{s}_{v_x}^{\psi_1^x} & \cdots & \tilde{s}_{v_x}^{\psi_N^x} \\
\tilde{s}_{q_x}^{v_x} & \tilde{s}_{q_x}^{q_x} & \tilde{s}_{q_x}^{\psi_1^x} & \cdots & \tilde{s}_{q_x}^{\psi_N^x} \\
\tilde{s}_{\psi_1^x}^{v_x} & \tilde{s}_{\psi_1^x}^{q_x} & \tilde{s}_{\psi_1^x}^{\psi_1^x} & \cdots & \tilde{s}_{\psi_1^x}^{\psi_N^x} \\
\vdots & \vdots & \vdots & \cdots & \vdots \\
\tilde{s}_{\psi_N^x}^{v_x} & \tilde{s}_{\psi_N^x}^{q_x} & \tilde{s}_{\psi_N^x}^{\psi_1^x} & \cdots & \tilde{s}_{\psi_N^x}^{\psi_N^x}
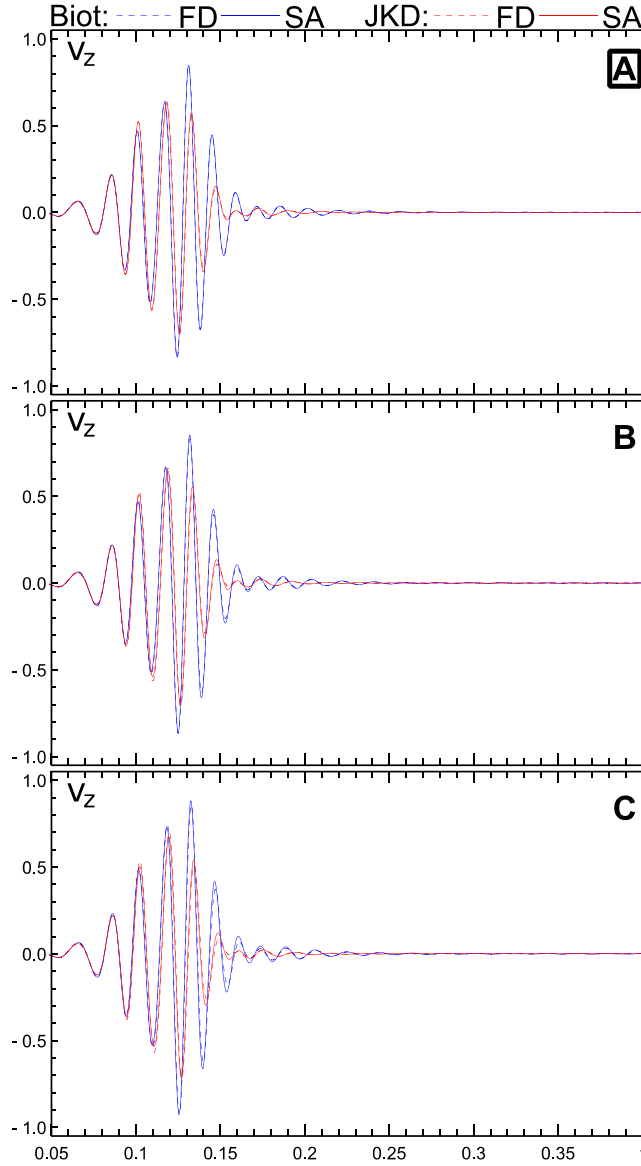\end{pmatrix}
\tag{64}
$$

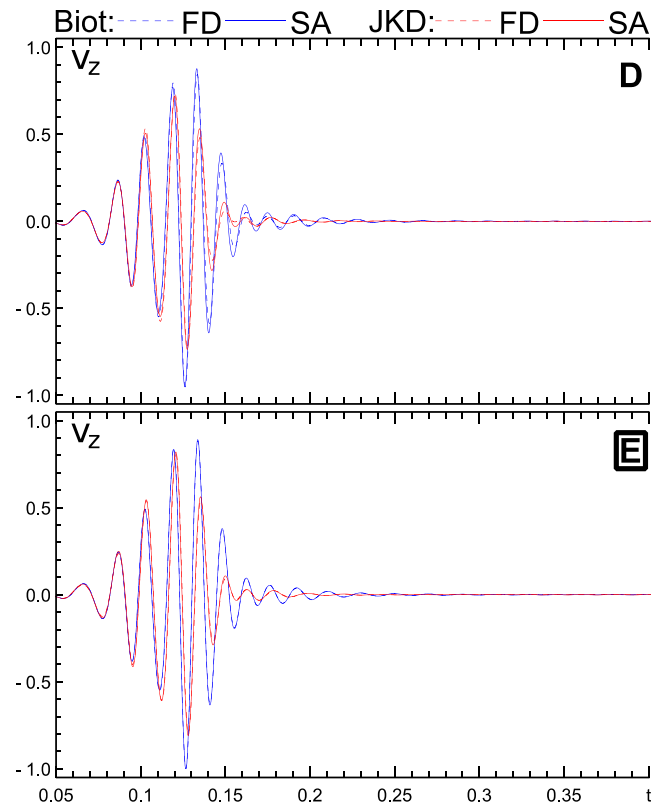**Figure 15.** The same as in Fig. 13 but for the v_z seismograms.

In the analogous matrix $\tilde{S}^z$, the index x in eq. (64) is simply replaced by index z. Using $^x\vec{Q}$ and $^z\vec{Q}$, and $\tilde{S}^x$ and $\tilde{S}^z$ in eqs (63) we obtain

$$
^x\vec{Q}^*\Big|^{m+1/2} =
\begin{pmatrix}
v_x^* & \big|^{m+1/2} \\
q_x^* & \big|^{m+1/2} \\
\psi_1^{x*} & \big|^{m+1/2} \\
\vdots & \\
\psi_N^{x*} & \big|^{m+1/2}
\end{pmatrix}
=
\begin{pmatrix}
\tilde{s}_{v_x}^{v_x} & \tilde{s}_{v_x}^{q_x} & \tilde{s}_{v_x}^{\psi_1^x} & \cdots & \tilde{s}_{v_x}^{\psi_N^x} \\
\tilde{s}_{q_x}^{v_x} & \tilde{s}_{q_x}^{q_x} & \tilde{s}_{q_x}^{\psi_1^x} & \cdots & \tilde{s}_{q_x}^{\psi_N^x} \\
\tilde{s}_{\psi_1^x}^{v_x} & \tilde{s}_{\psi_1^x}^{q_x} & \tilde{s}_{\psi_1^x}^{\psi_1^x} & \cdots & \tilde{s}_{\psi_1^x}^{\psi_N^x} \\
\vdots & \vdots & \vdots & \cdots & \vdots \\
\tilde{s}_{\psi_N^x}^{v_x} & \tilde{s}_{\psi_N^x}^{q_x} & \tilde{s}_{\psi_N^x}^{\psi_1^x} & \cdots & \tilde{s}_{\psi_N^x}^{\psi_N^x}
\end{pmatrix}
\begin{pmatrix}
v_x & \big|^{m-1/2} \\
q_x & \big|^{m-1/2} \\
\psi_1^x & \big|^{m-1/2} \\
\vdots & \\
\psi_N^x & \big|^{m-1/2}
\end{pmatrix}
\tag{65}
$$

and the analogous system for $^z\vec{Q}^*|^{m+1/2}$. Variables $v_x^*, q_x^*, , \psi_1^{x*}, \dots, \psi_N^{x*}$ and $v_z^*, q_z^*, , \psi_1^{z*}, \dots, \psi_N^{z*}$ at time level $m+1/2$ enter the non-stiff explicit scheme.

5 THE FD SCHEME

Let VX, VZ and QX, QZ be discrete grid values of v_x, v_z and q_x, q_z, respectively. Let TXX, TZZ, TXZ and FP be discrete grid values of σ_{xx}, σ_{zz}, σ_{xz} and fluid pressure p, respectively. For the grid values of the material parameters, we will use symbols defined by

**Figure 16.** The same as in Fig. 14 but for the v_z seismograms.

eqs (4)–(7) and (52). Fig. 1 shows positions of the field variables and material parameters in the grid cell. For brevity, we indicate material parameters as they appear in the equations for the smoothly heterogeneous medium. Denote the 4th-order accurate operators of the 1st spatial derivatives with respect to x and z coordinates:

$$D_x^{(4)} \Phi_{I,L}^n \equiv \frac{1}{h} \left[\frac{9}{8} \left(\Phi_{I+1/2,L}^n - \Phi_{I-1/2,L}^n \right) - \frac{1}{24} \left(\Phi_{I+3/2,L}^n - \Phi_{I-3/2,L}^n \right) \right]$$
$$D_z^{(4)} \Phi_{I,L}^n \equiv \frac{1}{h} \left[\frac{9}{8} \left(\Phi_{I,L+1/2}^n - \Phi_{I,L-1/2}^n \right) - \frac{1}{24} \left(\Phi_{I,L+3/2}^n - \Phi_{I,L-3/2}^n \right) \right] \tag{66}$$

The FD scheme consists of explicit FD formulas for updating the solid particle-velocity and relative fluid particle-velocity components, diffusive memory variables, stress components and fluid pressure:

$$VX_{I,L+1/2}^{m+1/2} = VX_{I,L+1/2}^* + \frac{1}{\langle S^x \rangle_{I,L+1/2}^z} \frac{\Delta}{h} \left\{ \langle F^x \rangle_{I,L+1/2}^z \left[D_x^{(4)} TXX_{I,L+1/2}^m + D_z^{(4)} TXZ_{I,L+1/2}^m \right] \right.$$
$$\left. + \langle G^x \rangle_{I,L+1/2}^z D_x^{(4)} FP_{I,L+1/2}^m \right\}$$
$$VX_{I,L+1/2}^* = \tilde{s}_{v_x;I,L+1/2}^{v_x} VX_{I,L+1/2}^{m-1/2} + \tilde{s}_{v_x;I,L+1/2}^{q_x} QX_{I,L+1/2}^{m-1/2} + \tilde{s}_{v_x;I,L+1/2}^{\psi_1^x} \psi_{1;I,L+1/2}^{x;m-1/2} + \ldots + \tilde{s}_{v_x;I,L+1/2}^{\psi_N^x} \psi_{N;I,L+1/2}^{x;m-1/2} \tag{67}$$

$$QX_{I,L+1/2}^{m+1/2} = QX_{I,L+1/2}^* - \frac{1}{\langle S^x \rangle_{I,L+1/2}^z} \frac{\Delta}{h} \left\{ \left(\langle R^x \rangle^z \left\langle \frac{G^x}{R^x} \right\rangle^z \right)_{I,L+1/2} \left[D_x^{(4)} TXX_{I,L+1/2}^m + D_z^{(4)} TXZ_{I,L+1/2}^m \right] \right.$$
$$\left. + \left(\langle P^x \rangle^z \langle G^x \rangle^z \right)_{I,L+1/2} D_x^{(4)} FP_{I,L+1/2}^m \right\}$$
$$QX_{I,L+1/2}^* = \tilde{s}_{q_x;I,L+1/2}^{v_x} VX_{I,L+1/2}^{m-1/2} + \tilde{s}_{q_x;I,L+1/2}^{q_x} QX_{I,L+1/2}^{m-1/2} + \tilde{s}_{q_x;I,L+1/2}^{\psi_1^x} \psi_{1;I,L+1/2}^{x;m-1/2} + \ldots + \tilde{s}_{q_x;I,L+1/2}^{\psi_N^x} \psi_{N;I,L+1/2}^{x;m-1/2} \tag{68}$$
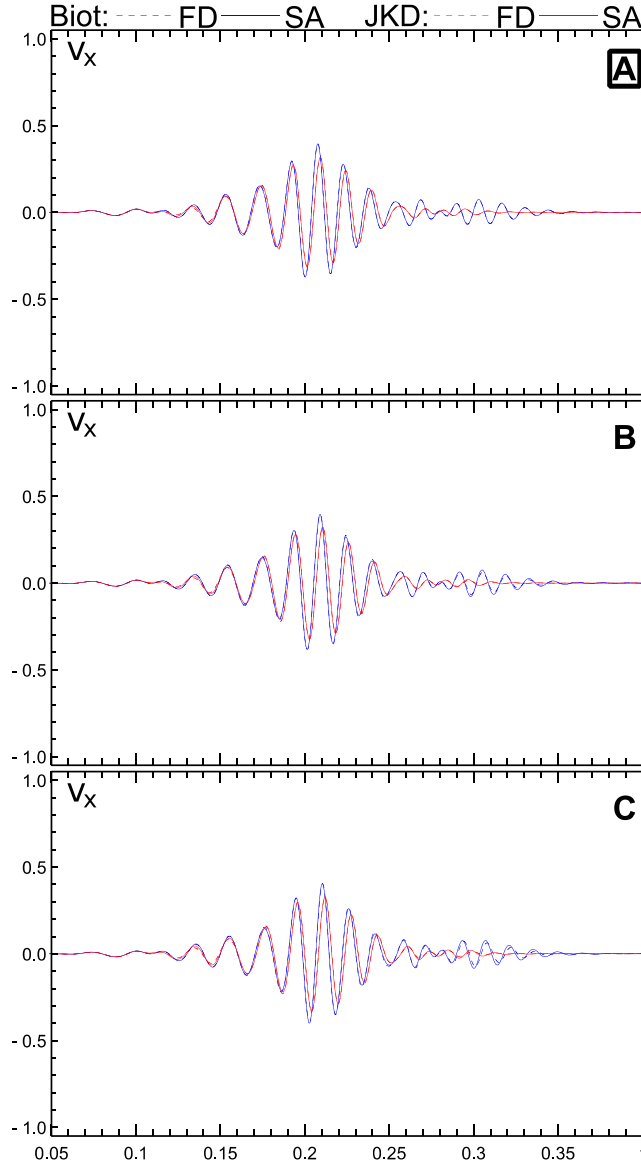
Figure 17. The v_x seismograms at receiver R2 in the models of the layer over half-space for the Biot's and JKD models calculated by our FD scheme and semi-analytical (SA) method. Labels A, B and C indicate the layer thicknesses and thus also positions of the layer–half-space interface in the FD grid (the grid being one and the same for all thicknesses/interface positions, see Fig. 6).

$$\psi_{n\,;\,I,\,L+1/2}^{x\,;\,m+1/2} = \psi_{n\,;\,I,\,L+1/2}^{x\,*} - \frac{1}{\langle S^x\rangle_{I,\,L+1/2}^z} \frac{\Delta}{h} \left\{ \left(\langle R^x\rangle^z \Big\langle \frac{G^x}{R^x}\Big\rangle^z \right)_{I,\,L+1/2} \left[D_x^{(4)}\, TXX_{I,\,L+1/2}^m + D_z^{(4)}\, TXZ_{I,\,L+1/2}^m \right] \right.$$

$$\left. + \left(\langle P^x\rangle^z \langle G^x\rangle^z \right)_{I,\,L+1/2} D_x^{(4)}\, FP_{I,\,L+1/2}^m \right\}$$

$$\psi_{n\,;\,I,\,L+1/2}^{x\,*} = \tilde{s}_{\psi_n^x;I,\,L+1/2}^{v_x}\, VX_{I,\,L+1/2}^{m-1/2} + \tilde{s}_{\psi_n^x;I,\,L+1/2}^{q_x}\, QX_{I,\,L+1/2}^{m-1/2} + \tilde{s}_{\psi_n^x;I,\,L+1/2}^{\psi_1^x}\, \psi_{1\,;\,I,\,L+1/2}^{x\,;\,m-1/2} + \ldots + \tilde{s}_{\psi_n^x;I,\,L+1/2}^{\psi_N^x}\, \psi_{N\,;\,I,\,L+1/2}^{x\,;\,m-1/2} \qquad (69)$$

$$n = 1, \ldots, N$$

$$TXZ_{I,\,L+1}^m = TXZ_{I,\,L+1}^{m-1} + \frac{\Delta}{h} \frac{\langle \mu\rangle_{I,\,L+1}^{Hxz}}{2} \left[D_z^{(4)}\, VX_{I,\,L+1}^{m-1/2} + D_x^{(4)}\, VZ_{I,\,L+1}^{m-1/2} \right] \qquad (70)$$
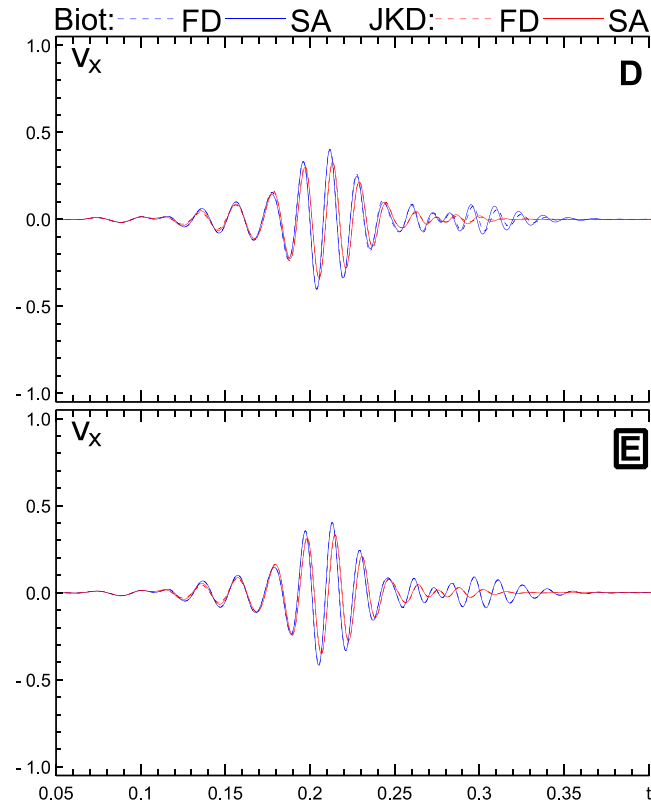
Figure 18. The same as in Fig. 17 but for the layer thicknesses/interface positions D and E.

$$FP^m_{I+1/2,\,L+1/2} = FP^{m-1}_{I+1/2,\,L+1/2} - \frac{\Delta}{h}\left\{\left(\frac{XP}{\Psi}\right)_{I+1/2,\,L+1/2} D^{(4)}_x VX^{m-1/2}_{I+1/2,\,L+1/2} + \left(\frac{ZP}{\Psi}\right)_{I+1/2,\,L+1/2} D^{(4)}_z VZ^{m-1/2}_{I+1/2,\,L+1/2}\right.$$

$$\left. + \left(\frac{1}{\Psi}\right)_{I+1/2,\,L+1/2} D^{(4)}_x QX^{m-1/2}_{I+1/2,\,L+1/2} + \left(\frac{1}{\Psi}\right)_{I+1/2,\,L+1/2} D^{(4)}_z QZ^{m-1/2}_{I+1/2,\,L+1/2}\right\} \tag{71}$$

The FD formulas for the remaining field components are specified in Appendix B.

In case of the non-zero constant resistive friction, $b = const > 0$, eqs (69) disappear and the second equations in (67) and (68) simplify:

$$VX^*_{I,\,L+1/2} = VX^{m-1/2}_{I,\,L+1/2} + \frac{1}{\langle P^x \rangle^z_{I,\,L+1/2}}\left[1 - \exp\left(-\Delta\,PHS_{I,\,L+1/2}\right)\right] QX^{m-1/2}_{I,\,L+1/2} \tag{72}$$

$$QX^*_{I,\,L+1/2} = \exp\left(-\Delta\,PHS_{I,\,L+1/2}\right) QX^{m-1/2}_{I,\,L+1/2} \tag{73}$$

with $PHS \equiv \langle P^x \rangle^z \langle H^x \rangle^z / \langle S^x \rangle^z$. Formulas for $VZ^*_{I+1/2,\,L+1}$ and $QZ^*_{I+1/2,\,L+1}$ are specified in Appendix B.

In Appendix C we briefly outline implementation of the free-surface boundary conditions and the source term.

6 NUMERICAL TESTS

Moczo *et al.* (2019) presented systematic numerical tests and comparisons for models with (i) zero resistive friction and (ii) non-zero constant resistive friction. The frequency range of interest was well below the Biot's characteristic frequency.

Here we present numerical tests of our discrete representation and FD scheme for the poroelastic medium with frequency-dependent permeability and resistive friction. We will denote medium/model with constant resistive friction as Biot's medium/model, whereas we will use abbreviation JKD for medium/model with frequency-dependent permeability and resistive friction. For modelling seismic wave propagation in the Biot's model we will use the FD scheme solving equations (3) and (50) with $B = b$ and $P_i = q_i$. For modelling seismic wave propagation in the JKD model we will use the FD scheme solving equations (3) and (50) with

$$B \equiv \frac{b}{\sqrt{\Omega}} \quad, \quad P_i \equiv \sum_{l=1}^{N} a_l\,\psi^i_l\,(t)\,. \tag{74}$$
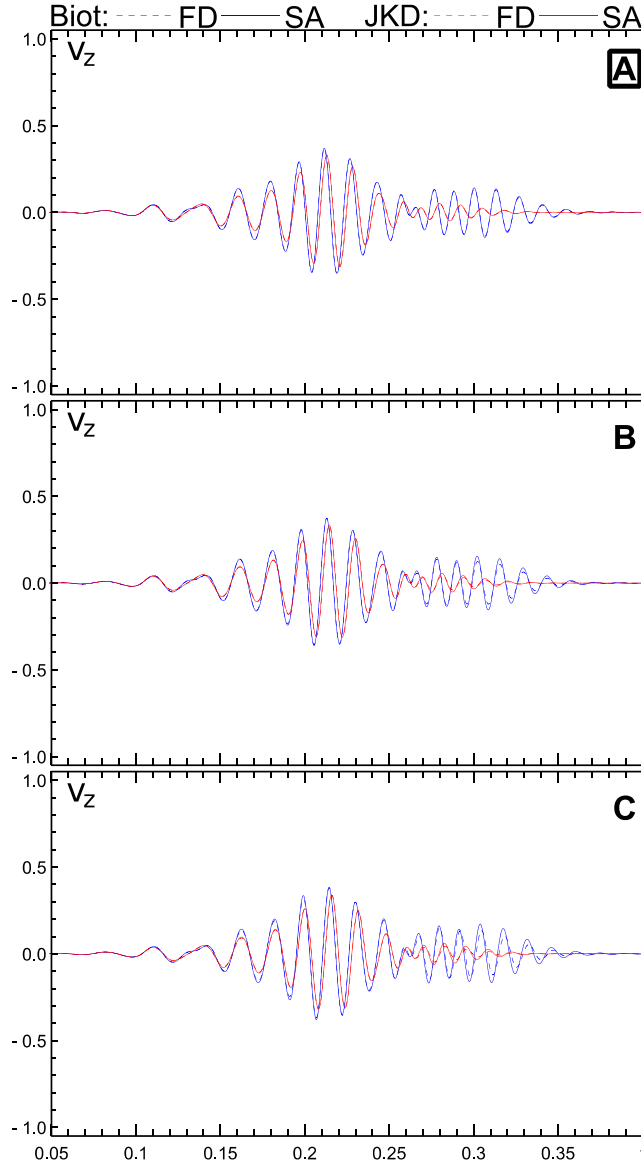
Figure 19. The same as in Fig. 17 but for the v_z seismograms.

We will test the FD scheme by comparing FD seismograms with those calculated using the semi-analytical method developed by Mesgouez & Lefeuve-Mesgouez (2009).

6.1 Homogeneous half-space—comparison with the semi-analytical solution

The upper panel of Fig. 2 shows configuration of the source and two receivers in the model of the homogeneous half-space. The upper panel also shows value of the intrinsic permeability κ_0 (for later comparison with the model of the layer over half-space). Values of all material parameters are listed in Fig 3. The high-permeability coarse sand makes the material of the half-space. Note that the dimensionless parameter n_J is not considered in the Biot's model.

The source is a single vertical load acting at the free surface and applied to both the solid matrix and fluid through the body-force terms in the equations of motion for the v_z and q_z components of the solid-matrix and relative fluid particle velocities. The source-time function is given by Ricker wavelet

$$s(t) = \frac{\sqrt{\pi}}{2}\left(a - \frac{1}{2}\right)e^{-a}; \qquad a = \left(\pi\,\frac{t - t_S}{t_P}\right)^2 \tag{75}$$
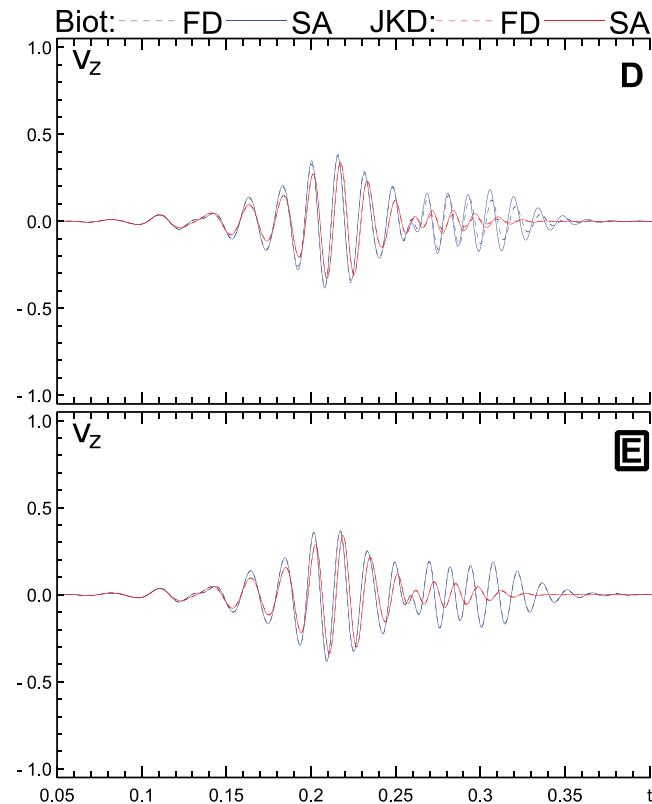
**Figure 20.** The same as in Fig. 18 but for the v_z seismograms.
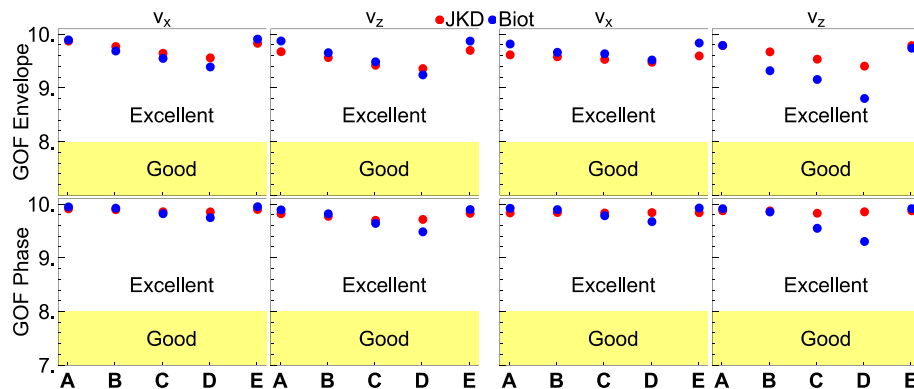
Figure 21. Envelope and Phase Goodness-of-fit (GOF) values quantifying level of agreement between the FD and SA solutions for the Biot and JKD medium alternatives of the model of the layer over half-space. GOF values are shown for the solid particle velocity components and for all five thicknesses of the layer and thus for all five positions of the layer-half-space interface in the fixed FD grid. The two left-hand columns show GOFs for receiver R1, the two right-hand columns for R2. The yellow and white zones indicate ranges of the excellent level of agreement and good level of agreement.
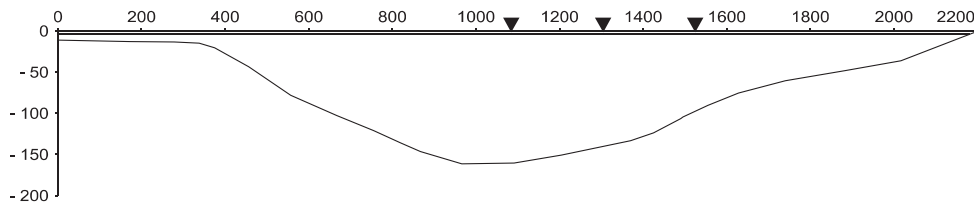
Figure 22. Geometry of the sediment-bedrock interface and interface between the horizontal surface sediment layer and underlying sediments. Sediments are water-saturated up to the free surface. Black triangles indicate positions of three selected receivers for which we individually compare seismograms for the Biot's and JKD model variants. The horizontal-to-vertical scale is 1:2, values along the horizontal and vertical axes are in meters. Material parameters are shown in Fig. 23.

Symbol	Units	4 m layer	irregular layer	halfspace
ρ_s	kg/m^3	2429	2650	2667
K_s	Pa	$37\cdot10^9$	$37\cdot10^9$	$37\cdot10^9$
fluid phase				
ρ_f	kg/m^3	1000	1000	1000
K_f	Pa	$2.25\cdot10^9$	$2.25\cdot10^9$	$2.25\cdot10^9$
η	$Pa\,s$	$1\cdot10^{-3}$	$1\cdot10^{-3}$	$1\cdot10^{-3}$
solid matrix (drained)				
K_m	Pa	$2.6\cdot10^8$	$1.14\cdot10^{10}$	$3.25\cdot10^{10}$
μ	Pa	$8.4\cdot10^7$	$9.295\cdot10^8$	$5.625\cdot10^9$
λ_m	Pa	$2.04\cdot10^8$	$1.0813\cdot10^{10}$	$2.875\cdot10^{10}$
ϕ		0.23	0.27	0.1
T		2.9	2.3	3
κ_0	m^2	10^{-8}	10^{-8}	10^{-12}
saturated porous medium (undrained)				
λ_c	Pa	$4.54\cdot10^8$	$1.6\cdot10^7$	$3.53\cdot10^9$
f_c	Hz	1.26	1.86	5305.16
n_J		8	8	8
velocities				
VP_{fast}^{inf}	m/s	2041	2727	4036
VP_{slow}^{inf}	m/s	170	849	858
VS^{inf}	m/s	204	668	1472

Figure 23. Material parameters and limit values of velocities of the fast *P* wave, slow *P* wave and *S* wave. The model of the sedimentary basin is shown in Fig. 22.
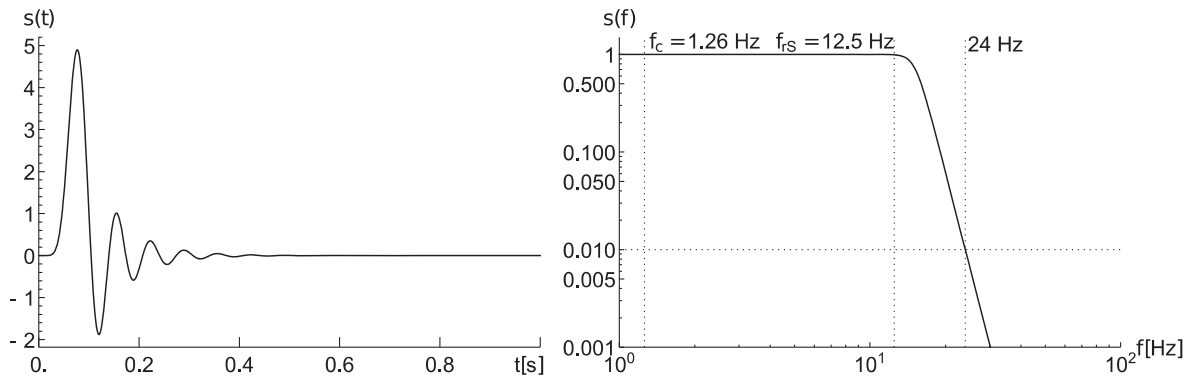
Figure 24. The source–time function of the incident wave, its normalized amplitude Fourier spectrum, Biot's characteristic frequency and frequency of the 1-D *S*-wave resonance in the thin surface layer. The model is shown in Fig. 22.
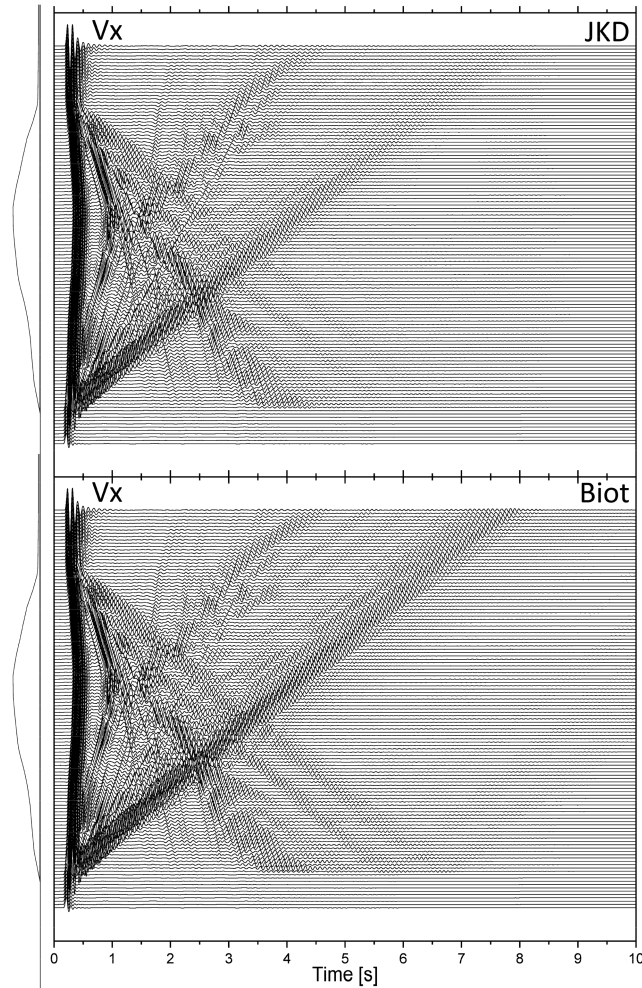
Figure 25. The v_x seismograms at receivers along the free surface of the sedimentary basin for the JKD (upper panel) and Biot's (lower panel) models.

The values of the free parameters t_P and t_S are shown in the bottom panel of Fig. 2 together with value of the Biot's characteristic frequency f_c. The Biot's frequency is well below the frequency at which the spectrum has its maximum.

We consider two receivers—R1 and R2 at the free surface. As indicated by the figure, due to the staggered grid, the grid position of the v_x component (solid square) is half grid spacing below the free surface whereas the grid position of the v_z component (solid circle) is exactly at the free surface. R1-v_x is at distance of 8.9 H and R1-v_z is at the horizontal distance of 9 H (H is the thickness of the layer in the model of the layer over half-space shown in the middle panel of Fig. 2.) The R2-v_x and R2-v_z distances are 26.9 H and 27 H, respectively.

Figure 4 shows the v_x and v_z seismograms at receiver R1 in the model of the homogeneous half-space for the Biot's and JKD models calculated by the FD scheme and semi-analytical (SA) method by Mesgouez & Lefeuve-Mesgouez (2009). We can see a very good agreement between the FD and SA seismograms for both model variants—Biot's and JKD. At the same time, as expected due to position of the Biot's characteristic frequency with respect to the source spectrum, some slight differences can be observed for the Biot's and JKD models.

Figure 5 shows the similar comparison for receiver R2. The level of agreement between the FD and SA seismograms is very good again. We can note a larger difference between the Biot's and JKD models. This can be explained by the larger travel distance between the source and R2 compared to the distance between the source and R1. The waves are more attenuated in the JKD model and this effect is cumulative—the larger the travel path, the larger the effect of attenuation.
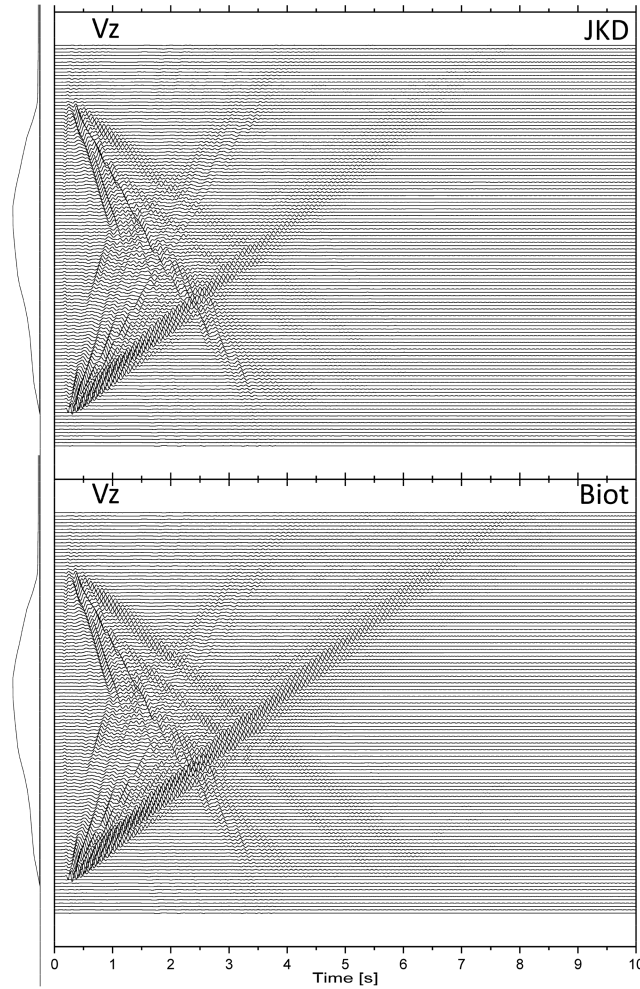
Figure 26. The same as in Fig. 25 but for the v_z seismograms.

## 6.2 Homogeneous layer over half-space—comparison with the semi-analytical solution

6.2.1 Reference model of the layer-half-space interface

The poroelastic material used for the homogeneous half-space in the previous subchapter is now used as the material of the horizontal homogeneous layer. The Porous rock from Fig. 3 makes the material of the half-space underlying the layer. The model and the source–receiver configuration are shown in the middle panel of Fig. 2. The middle panel also shows values of the intrinsic permeability κ_0 in the layer and half-space. The high permeability in the layer is an important feature of the model. Such permeability is typical for loose water-saturated sediments. The source and receivers are the same as in the model of the homogeneous half-space. The relatively small thickness of the layer is chosen in relation to the spectrum of the source signal: the thickness corresponds to a potential 1-D *S*-wave resonance at frequency of approximately 38.2 Hz at which the source signal has its spectral maximum.

Let us note the f_c in the coarse-sand layer being 1000 times smaller than f_c in the underlying porous rock. This difference is due to the values of the intrinsic permeability in the coarse sand and the porous rock. Géli *et al.* (1987) presented a nice overview of the values of the Biot's characteristic frequency and intrinsic permeability. We reproduce its essential part in Appendix D, Fig. D1.

The layer-half-space interface coincides with the grid plane consisting of grid positions of v_z, q_z and σ_{xz}. We denote this position of the interface in the grid as the A position—see Fig. 6.

Figure 7 shows the v_x and v_z seismograms at receiver R1 in the model of the layer over half-space for the Biot's and JKD models calculated by the FD scheme and semi-analytical method. We can see a very good agreement between the FD and SA seismograms for both model variants—Biot's and JKD. At the same time, we can see a considerable difference between seismograms for the Biot's and JKD models. The difference is larger than that for R1 in the model of the homogeneous half-space. The first part of the seismogram shows two signals quite close to each other, as in Fig. 4. This corresponds to the direct and first reflected waves. Then, in the second part, corresponding to multiple reflected and converted waves interfering, the discrepancy between the seismograms becomes larger. Recall that R1-v_x is at distance of 8.9 H and R1-v_z is at the horizontal distance of 9 H, where H is the thickness of the layer.
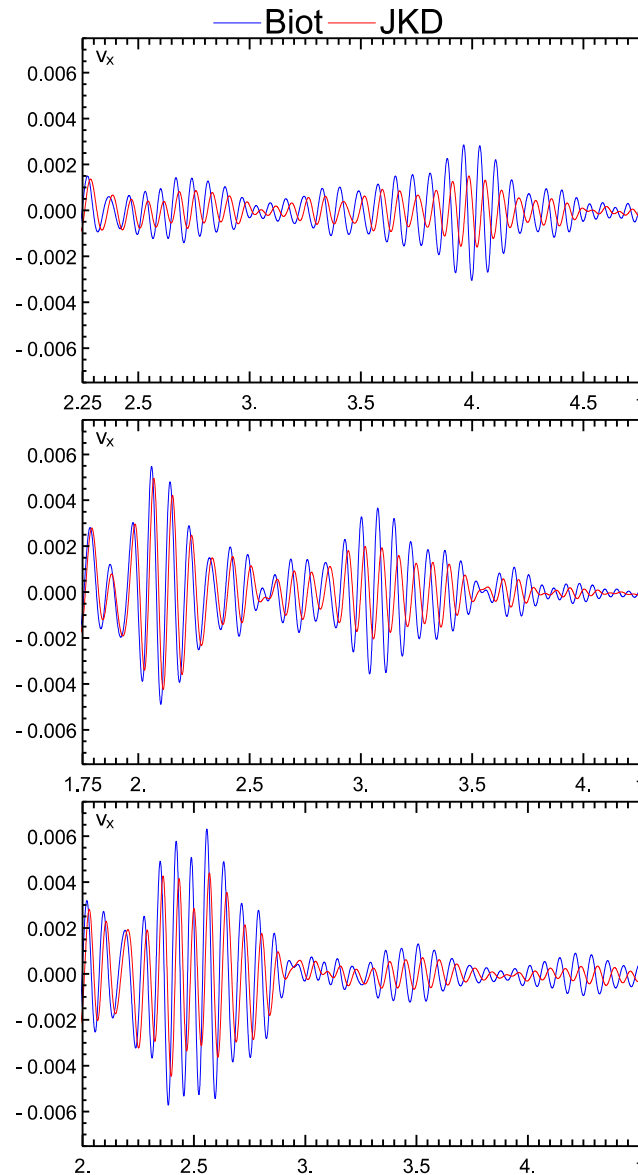
Figure 27. The v_x seismograms at three selected receivers (shown in Fig. 22) for Biot's and JKD models in selected time windows.

Figure 8 shows the similar comparison for receiver R2. The level of agreement between the FD and SA seismograms is very good again. As in the comparison between R1 and R2 in the model of the homogeneous half-space, we can note a larger difference between seismograms for the Biot's and JKD models at R2 compared to that at R1. Again, we attribute the larger difference to the cumulative effect due to larger travel path.

6.2.2 Testing the subcell resolution capability of the FD scheme

Moczo *et al.* (2019) carefully tested the subcell resolution of their FD scheme for the poroelastic medium with zero and non-zero constant resistive frictions. The presented FD scheme for the medium with the frequency-dependent permeability and resistive friction is substantially more complicated due to the diffusive approximation for the convolution term representing the resistive friction. Therefore, we need specific test of the subcell resolution of the scheme presented in this paper.

Figure 6 shows five positions of the horizontal layer-half-space interface in the grid, labelled A, B, C, D and E. Labels A and E are framed in order to indicate that the distance between the two positions is just one grid spacing h. The source and receivers are at the same positions in the grid in all five cases. Given the fixed position of the free surface, the five interface positions also mean five different thicknesses of the layer. In other words, the thickness of the layer varies in this set of five model modifications within one grid spacing which clearly is the relatively small scatter of layer thicknesses.

6.2.2.1 Scatter of wavefields due to variation in the layer thickness For each of the five layer thicknesses we calculated seismograms for the fixed positions of the source and receivers R1 and R2 with the semi-analytical method for both model variants—Biot's and JKD. The seismograms are shown in Figs 9–12. The scatter of seismogram for the five models is obvious in all figures which means that physically the five layer thicknesses (differing just within the size of one grid spacing $h = 0.09$ m) generate different wavefields.

6.2.2.2 Comparison of the SA and FD seismograms for the five layer thicknesses Figure 13 shows the v_x seismograms at receiver R1 in the models of the layer over half-space for the Biot's and JKD models calculated by the FD scheme and semi-analytical method. Labels A, B and C indicate the layer thicknesses and thus also positions of the layer-half-space interface in the FD grid (the grid being one and the same for all thicknesses/interface positions, see Fig. 6). Fig. 14 shows the same as Fig. 13 but for the layer thicknesses/interface positions D and E. Figs 15 and 16 show the same as Figs 13 and 14, respectively, but for the v_z seismograms. Analogously, Figs 17–20 show the same as Figs 13–16 but for receiver R2. We can see in Figs 13–20 very good level of agreement between the FD and SA solutions—the blue solid-line and dashed-line seismograms for the Biot's model are close to each other and clearly different from the red solid-line and dashed-line seismograms for the JKD model for all layer thicknesses, that is for all positions of the interface in one and the same fixed FD grid.

In addition to direct comparison of FD and SA seismograms we can directly quantify the level of agreement between the two solutions. Kristeková *et al.* (2008, 2009) developed the time–frequency envelope and phase goodness-of-fit (GOF) criteria based on the complete signal representation and previously introduced time-frequency envelope and phase misfit criteria (Kristeková *et al.* 2006). Figure 21 shows the envelope and phase goodness-of-fit (GOF) values quantifying level of agreement between the FD and SA solutions for the Biot's and JKD alternatives of the model of the layer over half-space. GOF values are shown for v_x and v_z, and for all five thicknesses of the layer, that is, also for all five positions of the layer–half-space interface in the FD grid. Clearly, for both types of the poroelastic medium (Biot's and JKD), five interface positions and both components, the level of agreement is excellent though there are small variations of the GOF values inside the range of the excellent level of agreement.

Overall, Figs 13–21 demonstrate for both Biot's and JKD model variants:

(1) very good level of accuracy of the developed FD scheme in all tested configurations and

(2) subcell resolution of the FD scheme—the capability to sense an interface position in between to grid planes (appearing in 2-D as grid lines), that is, within one grid spacing h.

7 EARTHQUAKE GROUND MOTION IN A LOCAL SURFACE SEDIMENTARY BASIN

Soft sediments and especially local surface sedimentary basins and valleys have been well known for anomalous earthquake ground motions, and, consequently, for increased damage in populated areas. We still do not sufficiently understand what the key controlling structural parameters are and, partially consequently, how to affordably and sufficiently accurately identify and characterize unfavourable site conditions and estimate their effects on earthquake ground motion. A major Research & Development project SIGMA (SeIsmic Ground Motion Assessment; Senfaute *et al.* 2015, Pecker *et al.* 2016, 2017), jointly organized by European energy giants EDF, AREVA, CEA and ENEL, addressed this crucial question—together with other problems. In the framework of the project, Kristek *et al.* (2018) developed methodology for calculating acceleration and corresponding earthquake ground motion characteristics at a site of interest assuming acceleration at a reference site for alternative basic configurations. Moczo *et al.* (2018) applied the methodology and performed extensive numerical investigations of earthquake ground motion for a set of models related to nuclear sites and specified by EDF (Electricité de France). The investigation included effects of a variety of structural parameters. It did not include the presence of the water-saturated sediments because there was no appropriate methodology available at that time. The logical need to look at effects of poroelastic material parameters on earthquake ground motion was, besides the methodological challenge, a reason for developing methodology presented in this paper.

Obviously, the problem requires a systematic investigation that must be addressed in a separate study. Here we present an illustrative example for one poroelastic modification of model of the sedimentary basin investigated in project SIGMA.

Figure 22 shows geometry of the model of the sedimentary basin, Fig. 23 shows values of material parameters and limit values (for infinite frequency) of velocities of the fast *P* wave, slow *P* wave and *S* wave. There are two water-saturated sediment layers inside the basin. The surface horizontal 4-m-thick layer is underlain by an irregular layer reaching in the central part of the basin depth of 160 m. We consider here two model variants—Biot's and JKD. The wavefield is excited by a vertically incident plane SV wave. Figure 24 shows the input signal, its amplitude Fourier spectrum, and values of the Biot's characteristic frequency ($f_c = 1.26$ *Hz*) and 1-D *S*-wave resonance frequency ($f_{rS} = 12.5$ Hz) in the thin surface layer. The source time function was obtained by low-pass filtering a discrete Dirac pulse with a 10-pole (sharp) 1-pass (causal) Butterworth filter with corner frequency of 15.145 Hz.

The first comparison of the velocity seismograms obtained for the Biot's and JKD model variants is shown in Figs 25 (v_x component) and 26 (v_z component). In Fig. 25 we can see the first arrival of the incident SV wave, reflected wave from the sediment-basement interface, laterally propagating waves inside the entire basin and horizontally propagating waves in the thin surface layer. The main difference between the Biot's and JKD models is in the amplitudes of the waves in the surface layer and can be well

seen in the later part of seismograms. They are more attenuated in the JKD model. The difference is also evident in seismograms of the v_z component in Fig. 26. A more detailed comparison is shown in Fig. 27 for three selected receivers atop the central (deepest) part of the sedimentary basin in the time windows [2.25, 4.75] s, [1.75, 4.25] s and [2.0, 4.5] s. The difference between the Biot's and JKD models is evident. We show just the selected time windows because seismograms for both models differ only slightly at the beginning.

This illustrative example for one of tens-to-hundreds of possible models of local surface sedimentary basins indicates that it is desirable to perform an extensive parametric study in order to find out when it is necessary to apply relatively complicated and computationally more demanding JKD model and when much simpler Biot's model is sufficient. The application of either model certainly depends on characteristics of seismic wavefield and earthquake ground motion that are to be investigated in practical applications.

8 CONCLUSIONS

We have developed a discrete representation of a strongly heterogeneous poroelastic medium with the JKD-model of the frequency-dependent resistive friction. We incorporated the representation in the FD scheme. The scheme has three important capabilities. The scheme

(1) can simulate seismic wave propagation in strongly heterogeneous poroelastic medium with (i) zero resistive friction, (ii) non-zero constant resistive friction and (iii) JKD model of the frequency-dependent permeability and resistive friction,

(2) is capable of sub-cell resolution, that is, allows for an arbitrary shape and position of an interface in the spatial grid and

(3) keeps computational efficiency of the scheme for a smoothly and weakly heterogeneous medium (medium without material interfaces) because the number of operations for updating stress-tensor, fluid pressure, solid particle velocities and fluid particle velocities is the same; the only difference is that it is necessary to evaluate averaged grid material parameters once before the FD simulation itself.

The developed representation further extends and proves the possibilities of the FD modelling of seismic wave propagation in strongly heterogeneous media—building up on developments by Moczo *et al.* (2002, 2014, 2019), Kristek & Moczo (2003), Kristek *et al.* (2017, 2019).

In the illustrative numerical example, we demonstrated differences between seismic wavefields and earthquake ground motion in the Biot's and JKD variants of the model of the surface sedimentary basin. The example indicates that it is desirable to perform an extensive parametric study in order to find out when it is necessary to apply relatively complicated and computationally more demanding JKD model and when much simpler Biot's model is sufficient.

ACKNOWLEDGEMENTS

REFERENCES

Alterman, Z.S. & Karal, F.C., 1968. Propagation of elastic waves in layered media by finite difference methods, *Bull. seism. Soc. Am.,* **58,** 367–398.

Balam, R.I., Iturrarán-Viveros, U. & Parra, J.O., 2018. Modeling poroelastic wave propagation in a real 2-D complex geological structure obtained via self-organizing maps, *Pure appl. Geophys.,* **175**(8), 2975–2986.

Bettina, A. & Wilmanski, K., 2014, *Continuum Thermodynamics Part II: Applications and Examples,* World Scientific Publishing.

Blanc, E., 2013, Time-domain numerical modeling of poroelastic waves: the Biot-JKD model with fractional derivatives, *Thèse*, Aix-Marseille Université, pp. 157.

Blanc, E., Chiavassa, G. & Lombard, B., 2012. Biot-JKD model: simulation of 1D transient poroelastic waves with fractional derivatives, *J. Comput. Phys.,* **237,** 1–20.

Carcione, J.M. & Quiroga-Goode, G., 1995. Some aspects of the physics and numerical modelling of Biot compressional waves, *J. Comp. Acoust.,* **3**(4), 261–280.

Cheng, A. H.-D., 2016. *Poroelasticity*. Springer.

Ditkin, V.A. & Prudnikov, L.P., 1965. *Manual on Operational Calculus*. Higher School, Moscow, in Russian.

Géli, L., Bard, P.-Y. & Schmitt, D., 1987. Seismic wave propagation in a very permeable water-saturated surface layer, *J. geophys. Res.,* **92,** 7931–7944.

Gregor, D., 2020, The finite-difference modelling of seismic wave propagation in the poroelastic medium – the 2D P-SV case, *PhD thesis*, Comenius University in Bratislava.

Hansen, N. R., 2018. ExpoRkit code(https://github.com/nielsrhansen/expoRkit).

Hanyga, A., 2001. Wave Propagation in Media with Singular Memory, *Math. Comput. Model.,* **34,** 1399–1421.

Itzá, R., Iturrarán-Viveros, U. & Parra, J.O., 2016. Optimal implicit 2-D finite differences to model wave propagation in poroelastic media, *Geophys. J. Int.,* **206**(2), 1111–1125.

Johnson, D. L., Koplik, J. & Dashen, R., 1987. Theory of dynamic permeability and tortuosity in fluid-saturated porous media, *J. Fluid Mech.,* **176,** 379–402.

Kappel, F. & Kuntsevich, A., 2000. An implementation of Shor's r-algorithm, *Comput. Optim. Appl.,* **15**(2), 193–205.

Karpfinger, F., Müller, T.M. & Gurevich, B., 2009. Green's functions and radiation patterns in poroelastic solids revisited, *Geophys. J. Int.,* **178,** 327–337.

Kristek, J. & Moczo, P., 2003. Seismic-wave propagation in viscoelastic media with material discontinuities: a 3D fourth-order staggered-grid finite-difference modelling, *Bull. seism. Soc. Am.,* **93,** 2273–2280.

Kristek, J., Moczo, P., Bard, P.-Y., Hollender, F. & Stripajová, S., 2018. Computation of amplification factor of earthquake ground motion for a local sedimentary structure, *Bull. Earthq. Eng.,* **16**(6), 2451–2475

Kristek, J., Moczo, P., Chaljub, E. & Kristekova, M., 2017. An orthorhombic representation of a heterogeneous medium for the finite-difference modelling of seismic wave propagation, *Geophys. J. Int.,* **208,** 1250–1264.

Kristek, J., Moczo, P., Chaljub, E. & Kristekova, M., 2019. A discrete representation of a heterogeneous viscoelastic medium for the finite-difference modelling of seismic wave propagation, *Geophys. J. Int.,* **217,** 2021–2034.

Kristekova, M., Kristek, J. & Moczo, P. 2008. The Fortran95 program package TF_MISFIT_and_GOF_CRITERIA and User's guide at http://www.nuquake.eu/Computer_Codes/

Kristekova, M., Kristek, J. & Moczo, P., 2009. Time-frequency misfit and goodness-of-fit criteria for quantitative comparison of time signals, *Geophys. J. Int.,* **178,** 813–825.

Kristekova, M., Kristek, J., Moczo, P. & Day, S. M., 2006. Misfit Criteria for quantitative comparison of seismograms, *Bull. seism. Soc. Am.,* **96,** 1836–1850.

Lemaitre, J. & Chaboche, J.-L., 1990. *Mechanics of Solid Materials,* Cambridge Univ. Press.

Liu, Y., 2014. Optimal staggered-grid finite-difference schemes based on least-squares for wave equation modelling, *Geophys. J. Int.,* **197,** 1033–1047.

Mesgouez, A. & Lefeuve-Mesgouez, G., 2009. Transient solution for multilayered poroviscoelastic media obtained by an exact stiffness matrix formulation, *Int. J. Numer. Anal. Meth. Geomech.,* **33,** 1911–1931.

Masson, Y.J. & Pride, S.R., 2010. Finite-difference modeling of Biot's poroelastic equations across all frequencies, *Geophysics,* **75**(2), N33–N41.

Masson, Y.J., Pride, S.R. & Nihei, K.T., 2006. Finite-difference modeling of Biot's poroelastic equations at seismic frequencies, *J. geophys. Res.,* **111,** B10305,

Moczo, P., Gregor, D., Kristek, J. & de la Puente, J., 2019. A discrete representation of material heterogeneity for the finite-difference modelling

of seismic wave propagation in a poroelastic medium, *Geophys. J. Int.,* **216**(2), 1072–1099.

Moczo, P., Kristek, J., Bard, P.-Y., Stripajová, S., Hollender, F., Chovanová, Z., Kristeková, M. & Sicilia, D., 2018. Key structural parameters affecting earthquake ground motion in 2D and 3D sedimentary structures, *Bull. Earthq. Eng.,* **16**(6), 2421–2450.

Moczo, P., Kristek, J. & Galis, M., 2014. *The Finite-Difference Modelling of Earthquake Motions: Waves and Ruptures,* Cambridge Univ. Press.

Moczo, P., Kristek, J., Vavryčuk, V., Archuleta, R. J. & Halada, L., 2002. 3D heterogeneous staggered-grid finite-difference modeling of seismic motion with volume harmonic and arithmetic averaging of elastic moduli and densities, *Bull. seism. Soc. Am.,* **92,** 3042–3066.

Pecker, A., Faccioli, E., Gürpinar, A., Martin, C. & Renault, P., 2016. Overview and lessons learned from a probabilistic seismic hazard assessment for France and Italy, *Deliverable* SIGMA-2016-D4-171.

Pecker, A., Faccioli, E., Gürpinar, A., Martin, C. & Renault, P., 2017. *An Overview of the Sigma Research Project: A European Approach to Seismic Hazard Analysis*. Springer.

Plyushchenkov, B.D & Turchaninov, V., 2000. Acoustic logging modeling by refined Biot's equations, *Inter. J. Modern Phys. C,* **12,** 305–396.

Senfaute, G., Pecker, A., Labbé, P., Sidaner, J.F., Berge-Thierry, C., Rzepka, J.P. & Contri, P., 2015, Contribution of the SIGMA research programme to analyses of uncertainties in seismic hazard assessment, in *Proceedings of the 9ième Colloque National AFPS,* Marne-la-Vallée, France, November 30–December 2.

Schanz, M., 2009. Poroelastodynamics: linear models, analytical solutions, and numerical methods, *Appl. Mech. Rev.,* **62**(3), 030803, doi:10.1115/1.3090831.

Sun, Y.-C., Hengxin, R., Zheng, X.-Z., Li, N., Zhang, W., Huang, Q. & Chen, X., 2019. 2-D poroelastic wave modelling with a topographic free surface by the curvilinear grid finite-difference method, *Geophys. J. Int.,* **218**(3), 1961–1982.

Zhang, W. & Chen, X. 2006. Traction image method for irregular free surface boundaries in finite difference seismic wave simulation, *Geophys. J. Int.,* **167**(1), 337–353.

Zhang, Y., Ping, P. & Zhang, S.-X., 2017. Finite-difference modeling of surface waves in poroelastic media and stress mirror conditions, *Appl. Geophys.,* **14**(1), 105–114.

Zhang, W., Zhang, Z. & Chen, X., 2012. Three-dimensional elastic wave numerical modelling in the presence of surface topography by a collocated-grid finite-difference method on curvilinear grids, *Geophys. J. Int.,* **190**(1), 358–378.

APPENDIX A

A_{qp}, C_{qp} are the $q \times p = (2N + 8) \times (2N + 8)$ matrices

$$A_{qp} \equiv \begin{pmatrix} 0_{N+2,\,N+2} & 0_{N+2,\,N+2} & A^{(1)}_{N+2,\,4} \\ 0_{N+2,\,N+2} & 0_{N+2,\,N+2} & A^{(2)}_{N+2,\,4} \\ A^{(3)}_{4,\,N+2} & A^{(4)}_{4,\,N+2} & 0_{4,\,4} \end{pmatrix} \tag{A1}$$

$$
A^{(1)}_{N+2,\,4} \equiv
\begin{pmatrix}
-\dfrac{\langle F^x\rangle^z}{\langle S^x\rangle^z} & 0 & 0 & -\dfrac{\langle G^x\rangle^z}{\langle S^x\rangle^z}\\[2ex]
\dfrac{\langle R^x\rangle^z\left\langle\frac{G^x}{R^x}\right\rangle^z}{\langle S^x\rangle^z} & 0 & 0 & \dfrac{\langle P^x\rangle^z\langle G^x\rangle^z}{\langle S^x\rangle^z}\\[2ex]
\dfrac{\langle R^x\rangle^z\left\langle\frac{G^x}{R^x}\right\rangle^z}{\langle S^x\rangle^z} & 0 & 0 & \dfrac{\langle P^x\rangle^z\langle G^x\rangle^z}{\langle S^x\rangle^z}\\[2ex]
\vdots & \vdots & \vdots & \vdots\\[1ex]
\dfrac{\langle R^x\rangle^z\left\langle\frac{G^x}{R^x}\right\rangle^z}{\langle S^x\rangle^z} & 0 & 0 & \dfrac{\langle P^x\rangle^z\langle G^x\rangle^z}{\langle S^x\rangle^z}
\end{pmatrix}
\tag{A2}
$$

$$
A^{(2)}_{N+2,\,4} \equiv
\begin{pmatrix}
0 & -\dfrac{\langle F^z\rangle^x}{\langle S^z\rangle^x} & 0 & 0\\[2ex]
0 & \dfrac{\langle R^z\rangle^x\left\langle\frac{G^z}{R^z}\right\rangle^x}{\langle S^z\rangle^x} & 0 & 0\\[2ex]
0 & \dfrac{\langle R^z\rangle^x\left\langle\frac{G^z}{R^z}\right\rangle^x}{\langle S^z\rangle^x} & 0 & 0\\[2ex]
\vdots & \vdots & \vdots & \vdots\\[1ex]
0 & \dfrac{\langle R^z\rangle^x\left\langle\frac{G^z}{R^z}\right\rangle^x}{\langle S^z\rangle^x} & 0 & 0
\end{pmatrix}
\tag{A3}
$$

$$
A^{(3)}_{4,\,N+2} \equiv
\begin{pmatrix}
-XX-\dfrac{XP\,XP}{\Psi} & -\dfrac{XP}{\Psi} & 0 & \cdots & 0\\[1.5ex]
0 & 0 & 0 & \cdots & 0\\[1ex]
-XZ-\dfrac{XP\,ZP}{\Psi} & -\dfrac{ZP}{\Psi} & 0 & \cdots & 0\\[1.5ex]
\dfrac{XP}{\Psi} & \dfrac{1}{\Psi} & 0 & \cdots & 0
\end{pmatrix},\quad
A^{(4)}_{4,\,N+2} \equiv
\begin{pmatrix}
0 & 0 & 0 & \cdots & 0\\
-\langle\mu\rangle^{Hxz} & 0 & 0 & \cdots & 0\\
0 & 0 & 0 & \cdots & 0\\
0 & 0 & 0 & \cdots & 0
\end{pmatrix}
\tag{A4}
$$

$$
C_{qp} \equiv
\begin{pmatrix}
0_{N+2,\,N+2} & 0_{N+2,\,N+2} & C^{(1)}_{N+2,\,4}\\
0_{N+2,\,N+2} & 0_{N+2,\,N+2} & C^{(2)}_{N+2,\,4}\\
C^{(4)}_{4,\,N+2} & C^{(4)}_{4,\,N+2} & 0_{4,\,4}
\end{pmatrix}
\tag{A5}
$$

$$
C^{(1)}_{N+2,\,4} \equiv
\begin{pmatrix}
0 & -\dfrac{\langle F^x \rangle^z}{\langle S^x \rangle^z} & 0 & 0 \\[2ex]
0 & \dfrac{\langle R^x \rangle^z \left\langle \dfrac{G^x}{R^x} \right\rangle^z}{\langle S^x \rangle^z} & 0 & 0 \\[3ex]
0 & \dfrac{\langle R^x \rangle^z \left\langle \dfrac{G^x}{R^x} \right\rangle^z}{\langle S^x \rangle^z} & 0 & 0 \\[3ex]
\vdots & \vdots & \vdots & \vdots \\[1ex]
0 & \dfrac{\langle R^x \rangle^z \left\langle \dfrac{G^x}{R^x} \right\rangle^z}{\langle S^x \rangle^z} & 0 & 0
\end{pmatrix}
\tag{A6}
$$

$$
C^{(2)}_{N+2,\,4} \equiv
\begin{pmatrix}
0 & 0 & -\dfrac{\langle F^z \rangle^x}{\langle S^z \rangle^x} & -\dfrac{\langle G^z \rangle^x}{\langle S^z \rangle^x} \\[2ex]
0 & 0 & \dfrac{\langle R^z \rangle^x \left\langle \dfrac{G^z}{R^z} \right\rangle^x}{\langle S^z \rangle^x} & \dfrac{\langle P^z \rangle^x \langle G^z \rangle^x}{\langle S^z \rangle^x} \\[3ex]
0 & 0 & \dfrac{\langle R^z \rangle^x \left\langle \dfrac{G^z}{R^z} \right\rangle^x}{\langle S^z \rangle^x} & \dfrac{\langle P^z \rangle^x \langle G^z \rangle^x}{\langle S^z \rangle^x} \\[3ex]
\vdots & \vdots & \vdots & \vdots \\[1ex]
0 & 0 & \dfrac{\langle R^z \rangle^x \left\langle \dfrac{G^z}{R^z} \right\rangle^x}{\langle S^z \rangle^x} & \dfrac{\langle P^z \rangle^x \langle G^z \rangle^x}{\langle S^z \rangle^x}
\end{pmatrix}
\tag{A7}
$$

$$
C^{(3)}_{4,\,N+2} \equiv A^{(4)}_{4,\,N+2}, \quad
C^{(4)}_{4,\,N+2} \equiv
\begin{pmatrix}
-XZ - \dfrac{XP\,ZP}{\Psi} & -\dfrac{XP}{\Psi} & 0 & \cdots & 0 \\[2ex]
0 & 0 & 0 & \cdots & 0 \\[1ex]
-ZZ - \dfrac{ZP\,ZP}{\Psi} & -\dfrac{ZP}{\Psi} & 0 & \cdots & 0 \\[2ex]
\dfrac{ZP}{\Psi} & \dfrac{1}{\Psi} & 0 & \cdots & 0
\end{pmatrix}
\tag{A8}
$$

S_{qp} is the $q \times p = (2N+8) \times (2N+8)$ matrix

$$
S_{qq} \equiv
\begin{pmatrix}
S^x_{N+2,\,N+2} & 0_{N+2,\,N+2} & 0_{N+2,\,4} \\
0_{N+2,\,N+2} & S^z_{N+2,\,N+2} & 0_{N+2,\,4} \\
0_{4,\,N+2} & 0_{4,\,N+2} & 0_{4,\,4}
\end{pmatrix}
\tag{A9}
$$

$$
S^x_{N+2,\,N+2} \equiv
\begin{pmatrix}
0 & 0 & -\dfrac{\langle H^x \rangle^z}{\langle S^x \rangle^z} a_1 & \cdots & -\dfrac{\langle H^x \rangle^z}{\langle S^x \rangle^z} a_N \\[2ex]
0 & 0 & \dfrac{\langle P^x \rangle^z \langle H^x \rangle^z}{\langle S^x \rangle^z} a_1 & \cdots & \dfrac{\langle P^x \rangle^z \langle H^x \rangle^z}{\langle S^x \rangle^z} a_N \\[3ex]
0 & -\bar{\Omega} & \dfrac{\langle P^x \rangle^z \langle H^x \rangle^z}{\langle S^x \rangle^z} a_1 + \left(\theta_1 + \bar{\Omega} \right) & \cdots & \dfrac{\langle P^x \rangle^z \langle H^x \rangle^z}{\langle S^x \rangle^z} a_N \\[3ex]
\vdots & \vdots & \vdots & \cdots & \vdots \\[1ex]
0 & -\bar{\Omega} & \dfrac{\langle P^x \rangle^z \langle H^x \rangle^z}{\langle S^x \rangle^z} a_1 & \cdots & \dfrac{\langle P^x \rangle^z \langle H^x \rangle^z}{\langle S^x \rangle^z} a_N + \left(\theta_N + \bar{\Omega} \right)
\end{pmatrix}
\tag{A10}
$$

$$S_{N+2,\,N+2}^z \equiv \begin{pmatrix} 0 & 0 & -\dfrac{\langle H^z\rangle^x}{\langle S^z\rangle^x}a_1 & \cdots & -\dfrac{\langle H^z\rangle^x}{\langle S^z\rangle^x}a_N \\[2ex] 0 & 0 & \dfrac{\langle P^z\rangle^x\langle H^z\rangle^x}{\langle S^z\rangle^x}a_1 & \cdots & \dfrac{\langle P^z\rangle^x\langle H^z\rangle^x}{\langle S^z\rangle^x}a_N \\[2ex] 0 & -\bar\Omega & \dfrac{\langle P^z\rangle^x\langle H^z\rangle^x}{\langle S^z\rangle^x}a_1 + \left(\theta_1 + \bar\Omega\right) & \cdots & \dfrac{\langle P^z\rangle^x\langle H^z\rangle^x}{\langle S^z\rangle^x}a_N \\[2ex] \vdots & \vdots & \vdots & \cdots & \vdots \\[2ex] 0 & -\bar\Omega & \dfrac{\langle P^z\rangle^x\langle H^z\rangle^x}{\langle S^z\rangle^x}a_1 & \cdots & \dfrac{\langle P^z\rangle^x\langle H^z\rangle^x}{\langle S^z\rangle^x}a_N + \left(\theta_N + \bar\Omega\right) \end{pmatrix} \tag{A11}$$

The abscissae $\theta_1, \ldots \theta_N$ are the same for the whole averaged model, whereas weights $a_1, \ldots a_N$ are calculated for each grid cell in the averaged model.

APPENDIX B

$$VZ_{I+1/2,\,L+1}^{m+1/2} = VZ_{I+1/2,\,L+1}^* + \frac{1}{\langle S^z\rangle_{I+1/2,\,L+1}^x}\frac{\Delta}{h}\left\{\langle F^z\rangle_{I+1/2,\,L+1}^x\left[D_x^{(4)}TXZ_{I,\,L+1/2}^m + D_z^{(4)}TZZ_{I,\,L+1/2}^m\right] + \langle G^z\rangle_{I+1/2,\,L+1}^x D_z^{(4)}FP_{I,\,L+1/2}^m\right\}$$

$$VZ_{I+1/2,\,L+1}^* = \tilde{s}_{v_z;\,I,\,L+1/2}^{v_z}\,VZ_{I+1/2,\,L+1}^{m-1/2} + \tilde{s}_{v_z;\,I+1/2,\,L+1}^{q_z}\,QZ_{I+1/2,\,L+1}^{m-1/2} + \tilde{s}_{v_z;\,I+1/2,\,L+1}^{\psi_1^z}\,\psi_{1;\,I+1/2,\,L+1}^{z;\,m-1/2} + \cdots$$
$$+ \tilde{s}_{v_z;\,I+1/2,\,L+1}^{\psi_N^z}\,\psi_{N;\,I+1/2,\,L+1}^{z;\,m-1/2} \tag{B1}$$

$$QZ_{I+1/2,\,L+1}^{m+1/2} = QZ_{I+1/2,\,L+1}^* - \frac{1}{\langle S^z\rangle_{I+1/2,\,L+1}^x}\frac{\Delta}{h}\left\{\left(\langle R^z\rangle^x\left\langle\frac{G^z}{R^z}\right\rangle^x\right)_{I+1/2,\,L+1}\left[D_x^{(4)}TXZ_{I,\,L+1/2}^m + D_z^{(4)}TZZ_{I,\,L+1/2}^m\right]\right.$$
$$\left. + \left(\langle P^z\rangle^x\langle G^z\rangle^x\right)_{I+1/2,\,L+1}D_z^{(4)}FP_{I,\,L+1/2}^m\right\}$$

$$QZ_{I+1/2,\,L+1}^* = \tilde{s}_{q_z;\,I+1/2,\,L+1}^{v_z}\,VZ_{I+1/2,\,L+1}^{m-1/2} + \tilde{s}_{q_z;\,I+1/2,\,L+1}^{q_z}\,QZ_{I+1/2,\,L+1}^{m-1/2}$$
$$+ \tilde{s}_{q_z;\,I+1/2,\,L+1}^{\psi_1^z}\,\psi_{1;\,I+1/2,\,L+1}^{z;\,m-1/2} + \cdots + \tilde{s}_{q_z;\,I+1/2,\,L+1}^{\psi_N^z}\,\psi_{N;\,I+1/2,\,L+1}^{z;\,m-1/2} \tag{B2}$$

$$\psi_{n;\,I+1/2,\,L+1}^{z;\,m+1/2} = \psi_{n;\,I+1/2,\,L+1}^{z;\,*} - \frac{1}{\langle S^z\rangle_{I+1/2,\,L+1}^x}\frac{\Delta}{h}\left\{\left(\langle R^z\rangle^x\left\langle\frac{G^z}{R^z}\right\rangle^x\right)_{I+1/2,\,L+1}\left[D_x^{(4)}TXZ_{I,\,L+1/2}^m + D_z^{(4)}TZZ_{I,\,L+1/2}^m\right]\right.$$
$$\left. + \left(\langle P^z\rangle^x\langle G^z\rangle^x\right)_{I+1/2,\,L+1}D_z^{(4)}FP_{I,\,L+1/2}^m\right\}$$

$$\psi_{n;\,I+1/2,\,L+1}^{z;\,*} = \tilde{s}_{\psi_n^z;\,I+1/2,\,L+1}^{v_z}\,VZ_{I+1/2,\,L+1}^{m-1/2} + \tilde{s}_{\psi_n^z;\,I+1/2,\,L+1}^{q_z}\,QZ_{I+1/2,\,L+1}^{m-1/2} + \tilde{s}_{\psi_n^z;\,I+1/2,\,L+1}^{\psi_1^z}\,\psi_{1;\,I+1/2,\,L+1}^{z;\,m-1/2} + \cdots + \tilde{s}_{\psi_n^z;\,I+1/2,\,L+1}^{\psi_N^z}\,\psi_{N;\,I+1/2,\,L+1}^{z;\,m-1/2}$$
$$n = 1, \ldots, N \tag{B3}$$

$$TXX_{I+1/2,\,L+1/2}^m = TXX_{I+1/2,\,L+1/2}^{m-1} + \frac{\Delta}{h}\left\{\left(XX + \frac{XP\,XP}{\Psi}\right)_{I+1/2,\,L+1/2}D_x^{(4)}VX_{I+1/2,\,L+1/2}^{m-1/2}\right.$$
$$+ \left(XZ + \frac{XP\,ZP}{\Psi}\right)_{I+1/2,\,L+1/2}D_z^{(4)}VZ_{I+1/2,\,L+1/2}^{m-1/2} + \left(\frac{XP}{\Psi}\right)_{I+1/2,\,L+1/2}D_x^{(4)}QX_{I+1/2,\,L+1/2}^{m-1/2}$$
$$+ \left.\left(\frac{XP}{\Psi}\right)_{I+1/2,\,L+1/2}D_z^{(4)}QZ_{I+1/2,\,L+1/2}^{m-1/2}\right\} \tag{B4}$$

$$
\begin{aligned}
TZZ^m_{I+1/2,\,L+1/2} = TZZ^{m-1}_{I+1/2,\,L+1/2} + \frac{\Delta}{h}\Bigg\{ & \left(XZ + \frac{XP\,ZP}{\Psi}\right)_{I+1/2,\,L+1/2} D^{(4)}_x VX^{m-1/2}_{I+1/2,\,L+1/2} \\
& + \left(ZZ + \frac{ZP\,ZP}{\Psi}\right)_{I+1/2,\,L+1/2} D^{(4)}_z VZ^{m-1/2}_{I+1/2,\,L+1/2} + \left(\frac{ZP}{\Psi}\right)_{I+1/2,\,L+1/2} D^{(4)}_x QX^{m-1/2}_{I+1/2,\,L+1/2} \\
& + \left(\frac{ZP}{\Psi}\right)_{I+1/2,\,L+1/2} D^{(4)}_z QZ^{m-1/2}_{I+1/2,\,L+1/2} \Bigg\}
\end{aligned}
\tag{B5}
$$

$$
VZ^*_{I+1/2,\,L+1} = VZ^{m-1/2}_{I+1/2,\,L+1} + \frac{1}{\langle P^z\rangle^x_{I+1/2,\,L+1}}\left\{1 - \exp\left[-\Delta\left(\frac{\langle P^z\rangle^x\langle H^z\rangle^x}{\langle S^z\rangle^x}\right)_{I+1/2,\,L+1}\right]\right\} QZ^{m-1/2}_{I+1/2,\,L+1}
\tag{B6}
$$

$$
QZ^*_{I+1/2,\,L+1} = \exp\left[-\Delta\left(\frac{\langle P^z\rangle^x\langle H^z\rangle^x}{\langle S^z\rangle^x}\right)_{I+1/2,\,L+1}\right] QZ^{m-1/2}_{I+1/2,\,L+1}
\tag{B7}
$$

APPENDIX C

Note on implementation of the traction-free conditions

The traction-free boundary conditions at the flat horizontal free surface are

$$
\sigma_{zz} = \sigma_{xz} = p = 0
\tag{C1}
$$

Application of the conditions (94) and averaged material parameters (Section 2.3) to the constitutive relations yields relations for the z-derivatives of the particle-velocity components:

$$
\begin{aligned}
\frac{\partial v_z}{\partial z} &= -\frac{XZ}{ZZ}\frac{\partial v_x}{\partial x} \\
\frac{\partial v_x}{\partial z} &= -\frac{\partial v_z}{\partial x} \\
\frac{\partial q_z}{\partial z} &= \left(ZP\frac{XZ}{ZZ} - ZP\right)\frac{\partial v_x}{\partial x} - \frac{\partial q_x}{\partial x}
\end{aligned}
\tag{C2}
$$

These relations are used at grid positions at and near the free surface. We have implemented two alternative approaches for updating field variables at and near the free surface—the stress-imaging approach and the adjusted finite-difference approximations (AFDA). Both approaches are explained, for example in the book by Moczo *et al.* (2014).

Note on implementation of the source term

The vertical load is implemented as

$$
\begin{aligned}
VZ^{m+1/2}_{I+1/2,L+1} &= VZ^{m-1/2}_{I+1/2,L+1} - \frac{\langle F^z\rangle^x}{\langle S^z\rangle^x}\frac{\Delta}{h^3}\frac{\partial s}{\partial t} \\
QZ^{m+1/2}_{I+1/2,L+1} &= QZ^{m+1/2}_{I+1/2,L+1} + \frac{\langle R^z\rangle^x\left\langle\dfrac{G^z}{R^z}\right\rangle^x}{\langle S^z\rangle^x}\frac{\Delta}{h^3}\frac{\partial s}{\partial t}
\end{aligned}
\tag{C3}
$$

in case of zero resistive friction, and

$$
\begin{aligned}
VZ^{m+1/2}_{I+1/2,L+1} &= VZ^*_{I+1/2,L+1} - \frac{\langle F^z\rangle^x}{\langle S^z\rangle^x}\frac{\Delta}{h^3}\frac{\partial s}{\partial t} \\
QZ^{m+1/2}_{I+1/2,L+1} &= QZ^*_{I+1/2,L+1} + \frac{\langle R^z\rangle^x\left\langle\dfrac{G^z}{R^z}\right\rangle^x}{\langle S^z\rangle^x}\frac{\Delta}{h^3}\frac{\partial s}{\partial t}
\end{aligned}
\tag{C4}
$$

in case of the non-zero resistive friction. Here s denotes a source-time function in particle displacement.

The incidence of a vertically propagating plane wave is simulated using standard Alterman–Karal decomposition (Alterman & Karal, 1968).

APPENDIX D

Application fields	Frequency range [Hz]	Material	exponent γ in $\kappa_0 = 10^{-\gamma}\ m^2$	f_c [Hz]
Earthquake engineering	$0-25$	Coarse sands and gravels	$8-10$	< 500
Geothermal fields seismic surveys	$0-20$	Hot water-saturated tuffs	$9-11$	< 500
Geotechnical recognition	$0-500$	Medium and fine sand silts	$10-13$	$< 10^4$
Sea bed acoustics	$1-4\cdot 10^3$	Sea bed sediments	$10-14$	$< 10^5$
Petroleum exploration well logging	$1-10^5$	Silts, clays, sandstones; oil- or gas-filled reservoirs	$13-16$ $14-17$	$< 10^6$

Figure D1. Frequency ranges, Biot's characteristic frequencies and intrinsic permeabilities for different application fields and poroelastic materials. Based on Table 1 published by Géli *et al.* (1987).